Extending the Timeline of Land Cover Data to Refine Our Understanding of Grassland Degradation in Northern China

by Brooke Iacone

B.S. in Geographic Information Science, May 2018, Rowan University
B.A. in Environmental Studies, May 2018, Rowan University

A Thesis submitted to

The Faculty of
The Columbian College of Arts and Sciences
of The George Washington University
in partial fulfillment of the requirements
for the degree of Master of Science

May 15, 2022

Thesis directed by

Ginger Allington
Assistant Professor of Geography

© Copyright 2022 by Brooke Iacone
All rights reserved

Dedication

This thesis is dedicated to Kavon—my best friend and partner in life. Thank you for supporting me endlessly. None of this would have been possible without you. I love you!

Acknowledgments

First and foremost, I want to thank and acknowledge my thesis adviser and mentor Dr. Ginger Allington for her unwavering support and encouragement throughout the completion of this thesis and my degree. Dr. Allington has been an incredibly dedicated adviser, an awesome teacher, and a friend during this journey. Her constructive feedback, willingness to help me learn and explore new methods, and genuine desire to see me succeed have been invaluable to my experience. The completion of this thesis would not have been possible without her constant support and guidance. I would also like to thank Dr. Ryan Engstrom for his contribution as a reader on this thesis and for all of his support along the way in developing the methods of this thesis, running the contextual features (several times!), and helping it all come together.

I also wish to express my deepest appreciation to my family, friends, and colleagues for their support throughout my graduate school journey. Thank you to the incredible and strong women of my family who serve as a source of constant inspiration—Golden Grams, mom, aunt Kelly, aunt Rose, Meredith and Paige—and to my dad and Kavon too! Thank you to Arina, my partner in crime, for all of your emotional support in completing this thesis, and to Sarah and Fox for keeping me sane as a teaching assistant! Thank you to Dr. David Rain, Dr. Moses Kansanga, Dr. Lisa Benton-Short, Dr. Michael Mann, Dr. Kelsey Nyland and all of the other amazing faculty members in the Geography Department for your guidance along the way.

Abstract of Dissertation

Extending the Timeline of Land Cover Data to Refine Our Understanding of Grassland Degradation in Northern China

Growing demand for resources from China's grasslands and the impacts of climate change continue to threaten the long-term health of these vital ecosystems. High-resolution CORONA imagery acquired by the United States through spy missions in the 1960's may provide critical insight into historic land cover conditions in prior decades, particularly in regions such as northern China where data from that era are scarce. Since the 1960's, the region has implemented many policy changes that have led to periods of intensified cultivation, grassland degradation and desertification and, in recent years, restoration. Most large-scale studies of land cover change only extend back to the 1980's and the advent of moderate resolution remotely sensed data. This timeline limits our ability to attribute changes prior to the 1980s or establish baseline conditions. CORONA imagery presents an opportunity to expand the timeline of available data on land use and land cover change in northern China. Here, we evaluate the feasibility and accuracy of using derived texture and spatial contextual features from CORONA imagery for classification.

In this study, four CORONA images were georeferenced using ground control points and Landsat TM imagery. Then, contextual features based on image texture characteristics were derived at several scales from a mosaic of the georeferenced images and combined with a Landsat MSS NDVI to create a multi-band image. We used an unsupervised clustering algorithm, paired with cluster statistics to derive a classified map of historic land cover containing eight classes, including three distinct dune types. The

results show that contextual features derived from Corona imagery are useful for extracting land cover types in far greater detail than other available datasets. This study represents the first land cover assessment of northern China for this time frame and will be valuable for future studies of land cover change.

Table of Contents

Dedication iii

Acknowledgments iv

Abstract of Thesis v

List of Figures x

List of Tables xii

Chapter 1: Introduction 1

1.1 Desertification 1

1.2 Grassland Degradation in Northern China 4

1.3 Grassland Policies in Inner Mongolia 6

1.4 Assessments of Grassland Degradation in Northern China 9

1.4.1 Historic Sources 11

Chapter 2: Study Area and Objectives 13

2.1 Study Area 13

2.2 Objectives 18

Chapter 3: Proposed Methodology for Georeferencing and Mosaicking Corona Imagery in Northern China 20

3.1 Introduction 20

3.1.1 Corona Missions 21

3.1.2 Georeferencing Corona Imagery 23

3.2 Study Area 25

3.3 Objectives 25

3.4 Data Collection 26

3.4.1 Corona Images 26
3.4.2 Other Imagery 28
3.5 Methodology 30
3.5.1 Preprocessing 30
3.5.2 Georeferencing 34
3.5.3 Mosaicking 40
3.5.4 Exporting the Mosaic 42
3.6 Assessment of the Final Mosaic 43
3.7 Discussion 46
3.7.1 Evaluating the Methods 46
3.7.2 Initial Assessment of Landscape Changes 48
3.7.3 Potential Uses of Corona Imagery 49
3.8 Conclusion 50
Chapter 4: Evaluating the Use of Contextual Featured Derived from Corona Imagery for Reconstructing Historic Land Cover Types in Inner Mongolia, China 51
4.1 Introduction 51
4.1.1 Corona Imagery 52
4.1.2 Contextual Feature Analysis 54
4.2 Objectives 57
4.3 Study Area 57
4.4 Data Collection 57
4.4.1 Corona Imagery 57

4.4.2 Other Imagery 58
4.5 Methods 59
4.5.1 Contextual Feature Analysis 59
4.5.2 Determining Appropriate Contextual Features 65
4.5.3 Unsupervised Classification 68
4.6 Results 69
4.6.1 Description of Land Cover Types and Assessment of Class Accuracy 72
4.6.2 Landsat MSS NDVI Evaluation 78
4.6.3 Accuracy Assessment 79
4.7 Discussion 82
4.7.1 Characterizing Naiman Banner's Landscape in 1970 82
4.7.2 Comparison to ESA WorldCover Data 83
4.7.3 Comparison to Historic Topographic Maps 84
4.7.4 Next Steps 89
4.8 Conclusion 91
Chapter 5: Conclusion 93
References 96

List of Figures

Figure 1: DaQingGuo National Protected Area, near Tongliao, Inner Mongolia 5

Figure 2: Typical Landscape in the Horqin Sandy Lands.....14

Figure 3: Study Area Overview Map.....16

Figure 4: Corona Imagery Global Coverage (1962-1972).....22

Figure 5: Landsat TM Imagery (1984) and Contemporary Imagery (2019) 29

Figure 6: Workflow for Georeferencing Corona Imagery.....31

Figure 7: Strip Diagram 33

Figure 8: Ground Control Points Shown Between Corona, Landsat TM, and Contemporary Imagery.....36

Figure 9: Location of Ground Control Points.....39

Figure 10: Georeferencing Polynomials 40

Figure 11: Skewed Cells After Georeferencing.....43

Figure 12: Final Mosaic of Naiman Banner, Inner Mongolia 45

Figure 13: Landsat MSS NDVI Results (1976).....59

Figure 14: Example of Pixel Window and Block Size 61

Figure 15: Workflow for Contextual Feature Analysis 63

Figure 16: Land Cover Dataset for Naiman Banner (1970) 71

Figure 17: Land Cover Classes.....72

Figure 18: Example of Fixed Dune Dominated by Grasses 76

Figure 19: Example of Semi-Fixed Dune 77

Figure 20: Example of Mobile Dunes.....78

Figure 21: Mosaic of Scanned Topographic Maps Developed by the U.S.S.R. (1970) 85

Figure 22: Comparison Between the Results of the Corona-Based Classification and USSR Topographic Maps, Centered on Naiman City 87
Figure 23: Comparison Between the Results of the Corona-Based Classification and USSR Topographic Maps, Centered on Western Sand Dunes 88

List of Tables

Table 1: Missions Details of Acquired Corona Imagery 27

Table 2: Corona Images Acquired for Georeferencing of Naiman Banner 27

Table 3: Types of Ground Control Points Selected 38

Table 4: Cell Size of Images After Georeferencing.....43

Table 5: Mean Accuracy of Final Corona Mosaic.....44

Table 6: Accuracy of Corona Images in Final Mosaic 44

Table 7: Contextual Feature Descriptions.....62

Table 8: Contextual Feature Outputs 64

Table 9: Contextual Features and Scales Used in Each Iteration of Unsupervised Classifications 67

Table 10: Area of Final Land Cover Classes 70

Table 11: Results of Accuracy Assessment of Contextual Feature-Based Unsupervised Classification on Corona Imagery 81

Chapter 1: Introduction

Land-use and land-cover (LULC) change due to anthropogenic impact and climate change is recognized as a major driver of global environmental change and one of the world's most pressing environmental concerns (Brovkin et al., 2013; Verburg et al., 2015). Human-induced LULC change has proven to contribute to greenhouse gas emissions, alter carbon and nitrogen cycles, and change the biophysical characteristics of the earth's surface through land degradation, further impacting climate cycles (de Noblet-Ducoudré et al., 2012; Pitman et al., 2009; Prestele et al., 2016). Additionally, LULC changes and the degradation of productive ecosystems have major impacts on human livelihoods due to loss of biodiversity and ecosystem services (Tao, 2014; Wang, 2011). Identifying the patterns and drivers of LULC, and the associated impacts to humans and the planet, involves analyzing complex socio-environmental systems that link human needs, behaviors, and actions to quantitative assessments of environmental change (Allington et al., 2017). In particular, analyzing the relationship between institutional changes and LULC changes is critical for understanding the impact of policy decisions, predicting the future health and functioning of a landscape, and effectively managing ecosystems.

1.1 Desertification

Nearly half of the Earth's ice-free land surface (about 52 million square kilometers) is drylands. Dryland ecosystems face great water scarcity due to high rates of evapotranspiration, and are therefore highly susceptible to land degradation and desertification (Rafferty & Pimm, 2020). The United Nations Environment Program (UNEP) estimates that desertification has already affected 36 million square kilometers

of the world's drylands (United Nations Environmental Program, 2022). Additionally, these areas are home to over two billion people worldwide and some of the world's poorest populations. The United Nations Convention to Combat Desertification estimates that desertification effects the lives of up to 250 million people, and 135 million may be displaced due to desertification by 2045 (United Nations Convention to Combat Desertification, 2017). Beyond human impact, dryland ecosystems support a wide variety of biodiversity, particularly soil biodiversity, that is threatened by desertification (International Union for Conservation of Nature, 2017). Desertification is one of the most pressing environmental issues associated with global LULC changes because loss of productive land threatens food security and the well-being of a large portion of the world's population and increases vulnerability to climate change (International Union for Conservation of Nature, 2017; Tao, 2014; Wang, 2011).

Desertification refers to a severe case of land degradation in which fertile land in arid, semi-arid and dry sub-humid environments experiences land use/land cover state changes due to natural and anthropogenic processes (D'Odorico et al., 2019; Sivakumar, 2007), leading to long-term loss of vegetation and nutrient-rich soil (Wang, 2011). This process begins with the removal of vegetation through drought and overgrazing which exposes bare soil to wind and water erosion. Additionally, unsustainable agriculture practices can deplete the soil's nutrients and result in loss of soil to erosion, impeding the ability of vegetation to recover (Schlesinger et al., 1990). This loss of vegetation and soil triggers feedback loops, resulting in structural changes to the presence of dominant vegetation types, reduction in soil water infiltration, accelerated erosion, and reduced soil fertility and accelerating the process of desertification (Bestelmeyer et al., 2015;

Schlesinger et al., 1990). These changes result in the long-term loss of biological productivity, ecological integrity, and the land's value to humans (Feng et al., 2015; IPBES, 2018). Land cover changes due to degradation often result in "regime shifts" in land use, since economic productivity is lost (Bestelmeyer et al., 2015). Perennial vegetation serves an important role in stabilizing dryland landscapes year-round by physically holding soils in place with vegetation roots and by maintaining equilibrium through the maintenance of a healthy soil biome which fosters for the regrowth of grasses (Bestelmeyer et al., 2015). Perennial vegetation cover of 50% or more is associated with near-total stabilization, but as coverage of perennial grasses decreases, erosion increases (Zhou et al., 2015). When grassland is removed, most commonly through overgrazing and the conversion of grassland to cropland, it exposes soils to wind erosion, and the loss of topsoil makes it difficult for grasses to recover. Often, annual species and woody shrubs begin to dominate the landscape, eventually simplifying and transforming the grasslands to shrubland (Liu et al., 2019). Therefore, woody encroachment is a key indicator of grassland degradation (Archer et al., 2017; Wang, 2011). Woody shrubs and annual grasses do not stabilize the landscape like perennial grasses do, and the surrounding soil are more susceptible to continued erosion, particularly in the non-growing season (Zhou et al., 2015). Conceptual models of desertification have shown that once grasslands have degraded to stabilized shrubland, it is extremely difficult for perennial grasses to recover (Schlesinger et al., 1990). However, some empirical work has shown that with the removal of livestock grazing and a substantial amount of recovery time, nutrient-rich soils and perennial grasses can recover in grassland systems (Allington & Valone, 2010).

1.2 Desertification and Grassland Degradation in Northern China

The grasslands in the Inner Mongolia Autonomous Region (IMAR), located in the north of China, are part of the largest grassland system in the world, the Eurasian Steppe (Wu et al., 2015). The Eurasian Steppe region as a whole has the highest indigenous plant and animal biodiversity amongst the world's grasslands, second only to the African savannah (Wu et al., 2015). The grasslands of northern China as a whole "extend from the western edge of Manchuria, across the Inner Mongolia Steppe and Loess Plateau of Shaanxi and Gansu provinces to the Tibet-Qinghai Plateau and the mountains and basins of Central Asia" (*Grasslands and Grassland Sciences in Northern China*, 1992). The grassland region has a semi-arid, cool climate spanning between moisture-rich forested ecosystems and dry desert ecosystems and was historically characterized by a plant community dominated by continuous cover of perennial grasses and forbs with scattered shrubs (Figure 1).

Figure 1

DaQingGuo National Protected Area, near Tongliao, Inner Mongolia

Note. This image depicts one of the only remaining large expanses of perennial grasses in this region of Inner Mongolia (Allington, 2015)

With a population that has nearly doubled in just 50 years and major economic reform since the opening of China's economy to the world in the 1970's, there is increased pressure on Inner Mongolia's grasslands to feed the growing population through agriculture and livestock production. According to Chinese government reports, 10% of China's grasslands were degraded in the 1970s, increasing to 30% in the 1980s and 50% in the 1990s. By the 2000s, about 90% of the grasslands were degraded, though the extent varies widely by region (Liu et al., 2019). In Inner Mongolia, the total coverage of grasslands decreased between the 1980s and 2000s. Dense grassland coverage consistently decreased areas of sparse vegetation cover dominated by annual grasses increased (Liu et al., 2019). China faces some of the most severe land degradation and desertification in the world, particularly in north China in the country's grasslands

(Wang, 2011). As of 2011, it was estimated that around one third of the land area of China was affected by desertification (Wang, 2011).

1.3 Grassland Policies in Inner Mongolia

Institutional changes in China's history, particularly within the last eighty years, have led to a series of policy changes that spurred periods of intensified cultivation and grazing pressure, and in recent years, restoration of grasslands. In order to properly analyze the historic, contemporary, or future conditions of grasslands in Inner Mongolia, it is important to understand the impact that various policy decisions have had within this socio-environmental system (SES).

Robinson et al. (2017), segregated the history of governance of Inner Mongolia's grasslands into five broad time periods—the tribal period (1000 BCE-1206CE), the feudal period (1206-1949), collectivization (1956-1978), opening and privatization (1980-2000), and the current era of policy dominance centered on restoration efforts (2000-present). For most of its history during the tribal period, the region that is now Inner Mongolia was part of the larger Mongolian plateau system, which operated largely as a pastoral economy dominated by nomadism (Grousset, 1970; Shelach, 2016). Between 1206 and 1949, beginning with the Mongolian Empire of Genghis Khan and ending with the Communist Revolution, a feudal model was implemented in which local residents managed land that was owned by regional rulers. For most of this period, grasslands were not severely degraded due to the low density of people and livestock and the consistent movement of people and animals. However, at the turn of the 20th century (roughly between 1912 and 1949) increased pressure for agricultural outputs led to the

first wave of grassland "reclamation" (i.e., conversion to crop production) and agricultural land tripled during this period (Yi & Zhang, 2011).

During the collectivization period, which was set into motion by the creation of IMAR in 1947 and the People's Republic of China in 1949, grasslands became collectively owned and managed under the "Land Revolution" and livestock was owned and managed at the township level (Robinson et al., 2017; Wu et al., 2015). Policies during this period, such as the "Grains-First" campaign (1959-1961), urged farmers to cultivate as much grain as possible and encouraged the conversion of grassland to cropland on large scales. Between 1959 and 1961 alone, it is estimated that 7,000 square kilometers of grassland were converted to cropland (Wu et al., 2015). During the collectivization period, livestock production also increased by 300% and many of the traditional grassland management practices that prevented long-term degradation were lost (Robinson et al., 2017).

The opening and privatization period began in 1978 during China's economic reforms that opened the economy to foreign investment. An unprecedented rate of economic development quickly led to profound landscape changes across the nation (Robinson et al., 2017; Wang, 2011; Wu et al., 2015). In 1983, the Chinese government disbanded the commune system with the establishment of the "Household Contract Responsibility System", and grasslands were de-collectivized shortly after through policies such as the Rangeland Law of 1985, which allowed for contractual allocation of grasslands for use by individual households (Ho, 2000). Rapid increases in fencing and allocation of pastures and livestock to individual households during this time led to large-scale fragmentation of the grassland systems, loss of mobility, and shrinking

of wetlands and surface water due to irrigation, leading to massive degradation (Li et al., 2012). By the end of the 1990's, nearly all herders and farmers in Inner Mongolia operated under private grassland contracts. The privatization of resources and integration into outside markets incentivized decision-making based on increased production rather than long-term conservation of grasslands (Robinson et al., 2017), and cultivated land in Inner Mongolia reached over seven million square kilometers (Wu et al., 2015). Some claim that degradation was at its worst during this period (Li et al., 2012).

The current era of "policy dominance", which began around the year 2000, is marked by the creation and implementation of a large number of policies and programs for combatting desertification and restoring grasslands (Robinson et al., 2017). While grasslands continue to be privately held, policy instruments are employed to manage herder activities and restore grasslands. As part of efforts to reduce dust storm activity and improve environmental conditions, several large-scale ecological and conservation programs were implemented in the early 2000's, including the Beijing-Tianjin Wind and Sand Source Control Project, Grain to Green Project, and Natural Forest Protection Project (Wu et al., 2015). The major policies directly targeted at grasslands include the Forbidden Grazing and Rotational Grazing Program (2010-ongoing), Return Grazing Land to Grassland (2003-2008 and 2014-ongoing), and the Grassland Eco-Compensation Program (2011-2015 and 2016- 2020). Generally speaking, these policies aimed to restore grasslands by reducing grazing pressure and controlling stocking rates of livestock. Additionally, various payment for ecosystem service (PES) models were implemented which compensated farmers and herders for their losses as a result of reduced herd sizes and grazing access (Li et al., 2018).

Some reports suggest that grasslands in northern China have responded positively to restoration efforts (Bryan et al., 2018). However, the long-term potential of grasslands in the area is still largely unknown due to the history of severe degradation and continual impacts of desertification (Hua & Squires, 2015; Robinson et al., 2017). Currently, land use practices are undergoing further change in Inner Mongolia due to the implementation of the "Separating Three Property Rights". This reform aims to consolidate rural lands through a market-oriented approach that allows for short-term rental of rural lands (Li et al., 2018). This reform has the potential to undermine much of the progress that has been made through restoration efforts and PES policies because studies have found that farmers tend to overexploit rented land over owned land (Gao et al., 2012), and cannot benefit from PES subsidies as renters, disincentivizing them to reduce grazing intensity (Huang et al., 2011).

1.4 Assessments of Grassland Degradation in Northern China

While there is evidence that these periods of institutional change and land use intensification have impacted the grasslands of northern China, particularly in Inner Mongolia, the quantification of those changes and current status remains unclear. While visual interpretation and field investigation remain commonplace for measuring grassland conditions, these methods are time-consuming and expensive, and an increasing amount of research has focused on utilizing remotely sensed imagery (Brogaard & Prieler, 1998; Dong et al., 2011; Guo & Wen, 2020; Li et al., 2012; Li et al., 2013, 2015, 2017; Miyasaka et al., 2016; Runnström, 2000; Wang et al., 2012; Wen et al., 2020; Xu et al., 2018; Zhou et al., 2015). Regularly acquired satellite imagery has become an effective tool for large-scale ecological and environmental monitoring, particularly land cover

changes. Grassland degradation is typically monitored by measuring the health and extent of vegetation, which is accomplished using vegetation indexes (Li et al., 2017). Long-term analyses that detect change over time can also shed light on the status of grasslands through periods of intensified degradation, and more recently have been used to help measure the success of restoration efforts (Dong et al., 2011; Wang et al., 2012).

The status of grasslands has been assessed with several different spectral measures. One study utilized the Normalized Difference Vegetation Index (NDVI) and climate data and determined that overall greenness in northern China increased between 1982 and 2011, while only a small percentage of total land area (3.7%) experienced significant degradation (An et al., 2014). Similarly, Wang et al. found that land degradation in northern China increased at a rapid rate between 1975 and 1990 and continued, but at a slower rate, between 1990 and 2000. Between 2000 and 2010, degradation decreased (Wang et al., 2011). Other studies have utilized measures such as albedo for detecting desertification (Wen et al., 2020), and object-based classification for categorizing land uses (Miyasaka et al., 2016).

However, the dominant spectral approaches for monitoring and assessing the condition of grasslands over time may not be sufficient for understanding degradation and long-term recovery of grasslands. First, land cover classifications that segment semi-arid environments into a few broad cover types such as barren/sparsely vegetated areas and grassland omit complexities found within classes. These broad cover types do not capture the gradient of vegetation coverage, which, as described earlier, is essential for understanding the stability of the landscape. A broad cover type such as grassland also does not shed light on the composition of the vegetation, whether it is perennial, annual,

or woody shrub. These complexities are essential for understanding the progression of desertification, state of the soil, and susceptibility to wind erosion. And second, dominant spectral approaches for monitoring grassland recovery have predominantly relied on greenness and vegetation indexes. These measure, while useful, again do not inform on the recovery of the landscape in terms of vegetation composition.

Further, current remote sensing analyses of grassland degradation are limited by the availability of regularly acquired, moderate resolution satellite imagery. Due to these data limitations, most studies cannot extend their analysis prior to the late 1970s, and more commonly do not extend prior to the mid-1980s. However, as described previously, grassland degradation was already occurring during this time, both slowly over the long-term and then much more rapidly by the early 1980s with the privatizing of China's grasslands. Therefore, there is a significant gap in our understanding of the condition of grasslands prior to the most intense period of degradation in China's history to date.

1.4.1 Historic Sources

Other sources of information, such as historic maps, aerial photography and field accounts, may be useful for extending the timeline of information on the condition of landscapes over time. However, these sources are often scarce, particularly outside of the United States. Corona imagery was acquired by the United States between 1959 and 1972 as part of a classified program to gain military intelligence during the Cold War. The imagery was acquired globally with particular focus on political hotspots such as China, the Soviet Union, and the Middle East (National Reconnaissance Office, n.d.). Corona imagery is high spatial-resolution, panchromatic, single-band imagery; it lacks the spectral information that is typically used to derive land cover classifications and assess

land degradation trends. However, previous studies have successfully made use of Corona imagery to assess land cover and detect changes to forests and agriculture over time using methods such as digitization (Andersen, 2006; Coskun Hepcan, 2013; Franklin et al., 2005; Munteanu et al., 2020; Y. Zhang et al., 2020), object-oriented image segmentation (Gurjar & Tare, 2019; Nita et al., 2018; Rendenieks et al., 2020), and utilizing texture analysis to derive values for a classifier (Gurjar & Tare, 2019; Saleem et al., 2018; Shahtahmassebi et al., 2017; Song et al., 2015). However, few studies have utilized Corona imagery in semi-arid environments, nor have any studies attempted to characterize grasslands or detect dryland vegetation. Additionally, Corona imagery is difficult to utilize due to challenges associated with preparing the data for use. The literature surrounding their preparation is often not detailed enough to replicate (Hamandawana et al., 2007; Sohn et al., 2004). Corona imagery contains no spatial reference and must be georeferenced manually. This can be difficult in rural areas with few reference ground control points and variable topography. They also contain several types of geometric and brightness distortions that must be accounted for (Hamandawana et al., 2007; Sohn et al., 2004). Corona imagery represents a unique opportunity to characterize landscapes in northern China prior to intense degradation and expand the timeline of available knowledge, however, new methodologies are needed to assess their use in semi-arid environments for extracting information about grasslands.

Chapter 2: Study Area and Objectives

This thesis aims to characterize the landscape of Naiman Banner, China in 1970, in order to refine our understanding of grassland degradation in this region and extend the timeline of land cover information.

2.1 Study Area

Naiman Banner, located at E120°19′40″–121°35′40″, N42°14′10″–43°32′20″, is situated in the eastern portion of the Inner Mongolian Autonomous Region of China and on the southern edge of the Horqin Sandy Land District. Horqin, more broadly, is the largest of China's sandy lands and is situated in the western portion of the northeast area of China in the transition zone between the Northeast Plain and the Mongolian Plateau (Wang, 2011). It is a semi-arid ecosystem that serves as a transitional zone between semi-pastoral areas to the south and pastoral areas to the north (L. Xu et al., 2018). It is characterized by its undulating sand-dunes and meadows. The soils here are light and loose, making them highly susceptible to wind erosion. Due to dune movement caused by wind, the topography in Horqin is dynamic and varying (Wang, 2011). In 1985, degraded grasslands accounted for 14% of all land in the Horqin Sandy Lands. By 1992, degraded grasslands increased to nearly 20%. In 2013, the degraded area was estimated at 12%. However, while degraded grasslands have decreased proportionally, the total amount of grasslands in Horqin have decreased between these time periods by approximately 17% (Wang, 2011).

Figure 2

Typical Landscape in the Horqin Sandy Lands

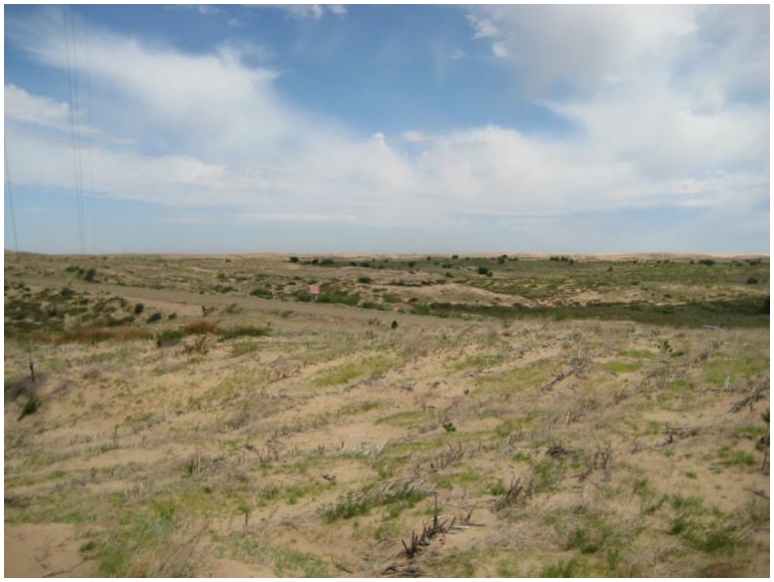

Note. This image depicts spotty grass and shrub coverage mixed with loose, sandy soil (Allington, 2009)

Naiman Banner falls within the Tongliao City prefecture. Tongliao City is located about 150 kilometers to the northeast (Wang, 2011). The elevation is high in the south (400–500-meter average elevation) and low in the north (below 300-meter average elevation). The central region, which is the focus of this analysis, ranges in elevation from 300 to 400 meters, with the highest elevation along the western side of the banner where the landscape is much sandier with highly mobile dune fields (Wang, 2011). Elevation slopes downward from west to east, transitioning from mobile dunes to semi-fixed and fixed dunes and then to flatter, gently sloping meadows. Vegetation cover exists in a gradient across the landscape from west to east, aligned with the gradient of dune stabilization from mobile to fixed (Zhou et al., 2015). Fixed dunes are defined by high vegetation coverage which stabilizes the dunes and prevents wind erosion. Semi-fixed dunes typically have vegetation coverage of less than 50%, and mobile dunes are

sparsely vegetated or barren with loose, sandy soil that is highly mobile and susceptible to wind erosion (Zhou et al., 2015). From west to east, this gradient transitions from bare sand to patchy vegetation coverage to shrubby and then mostly continuous grass coverage and cultivated areas (Figure 2). The soil in the central area is mainly chestnut soil, which is found to have been mostly degraded to sandy soil with coarser texture and looser structure (Zhou et al., 2015). The landscape was historically dominated by perennial grasses, but is now dominated by secondary vegetation such as shrubs and annual herbaceous plants including *Caragana microphylla, Artemisia halodendron, Artemisia frigida, Mellissitus ruthenicus, Cleistogenes squarrosa,* and *Setaria viridis* (Zhou et al., 2015).

Most of the present-day settlements, cropland, and gazing areas exist in the east on the flatter, more fertile land closer to water sources (Miyasaka et al., 2016; Zhou et al., 2015). The population of Naiman Banner in 2020 was 375,312, with the majority of the population living in and south of the city of Naiman, located at the southern border of the study area and centrally in the banner (China National Bureau of Statistics, 2020). It is estimated that agriculture covers nearly 50% of Naiman's land area today (Xu et al., 2018). The study area focuses on the central region of Naiman banner, covering 2324 square kilometers, or roughly a third of total area of the banners (Figure 3).

Figure 3
Study Area Overview Map

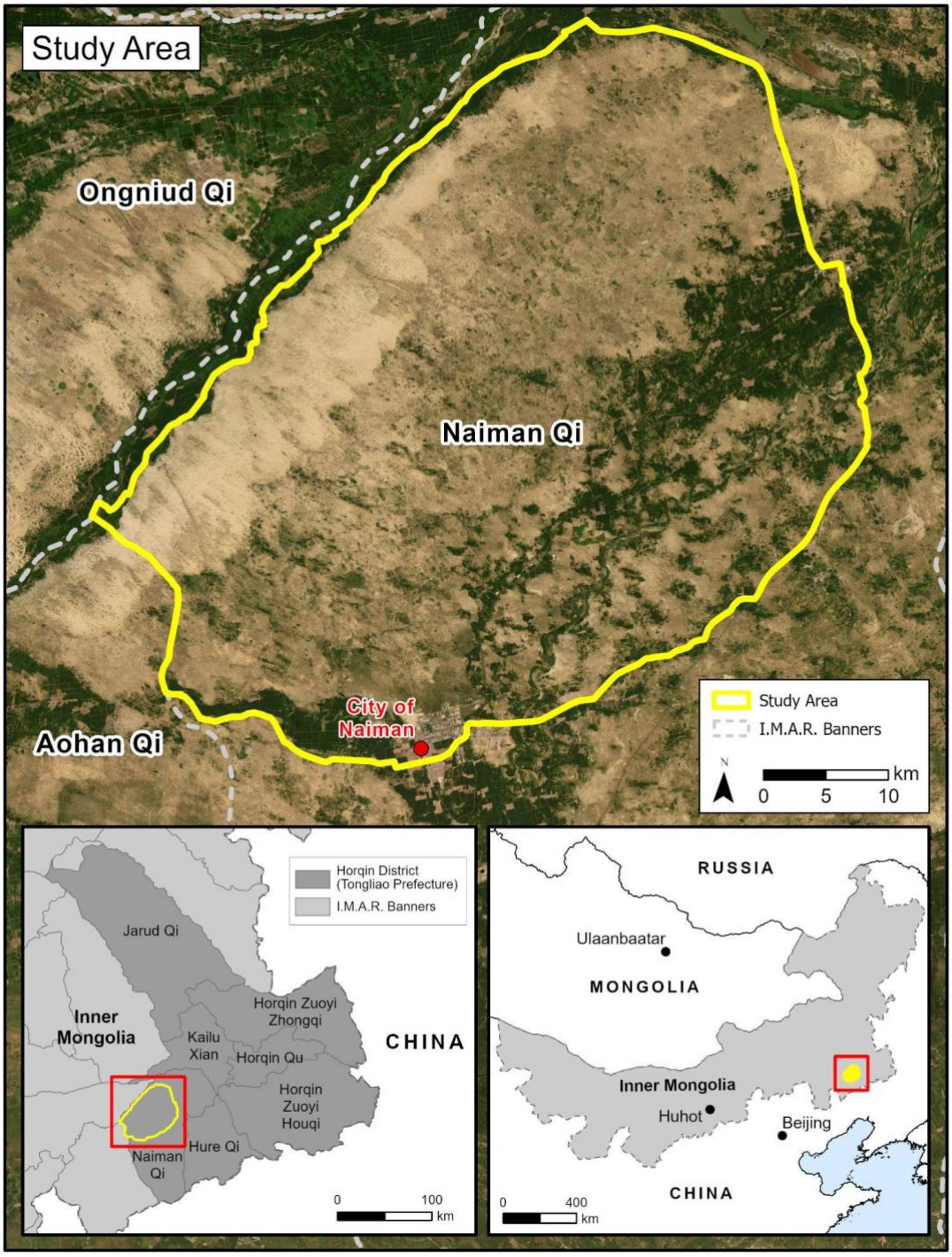

Note. The study area is shown within Naiman Banner, within the Tongliao City prefecture, and within the People's Republic of China

Naiman Banner faces some of the most severe grassland degradation in all of northern China (Li et al., 2015; Wen et al., 2020), and the trajectory of degradation over time generally follows that of the Horqin Sandy Lands and northern China, with the most intense period of degradation occurring between the mid-1980s and late-1990s (Li et al., 2015). There is evidence that the landscape has been recovering in recent years due to several grassland conservation programs in the region (Li et al., 2015; Xu et al., 2018; G. Zhang et al., 2012). This includes the Grain for Green Program (beginning 1999), the West Development Strategies (beginning 1999), the Beiijing and Tianjin the Grazing Withdrawal Program (beginning 2003) and the Ecological Subsidy and Award System (beginning 2011) (Li et al., 2017). Many of these efforts focus on tree planting and reduced grazing intensity in order to restore grasslands and minimize sandy dune encroachment. However, agricultural land has steadily increased over time, and despite restricting grazing in certain areas, the number of livestock has also increased. The groundwater table is also decreasing, which could lead to future problems associated with desertification despite all of these recent efforts (Li et al., 2017). Additionally, much of the area that has experienced significant recovery is located in the southern portion of Naiman Banner (Xu et al., 2018; Zhang et al., 2012), not in the central region which is considered the most severely degraded in all of Naiman, and Horqin at large (Li et al., 2017; Wen et al., 2020). Various sand-fixing measures have also been implemented here to help stabilize the landscape, some of which have been around since the mid-1970's (Miyasaka et al., 2016). These measures often include building physical sand barriers, corn straw fence belts, and checkboard patterns of wheat straw on highly mobile dunes (Miyasaka et al., 2016).

2.2 Objectives

The overarching objective of this work is to generate new datasets that will extend the timeline of available data for monitoring grassland degradation and recovery dynamics in northern China. Focusing on a highly degraded region of Naiman Banner, Inner Mongolia, this work will characterize the landscape conditions prior to the massive privatization and land use intensification that occurred in the 1980s and 1990s. Little is known about the health and extent of grassland degradation in Naiman Banner prior to the 1980s due to the lack of available satellite imagery from that time period. In order to characterize the landscape during previous time periods, it is necessary to make use of alternative historic sources of information such as Corona imagery. This imagery represents a unique opportunity to visualize and qualitatively assess landscape conditions at an earlier timepoint. To date, no historic land cover datasets exist for this time period. However, there are challenges associated with using Corona imagery which present a need for new methods in order to extract land cover information. The literature surrounding the use of Corona imagery is sparse and few studies have utilized Corona imagery in more rural, semi-arid environments, or to detect a range of vegetation coverage types. Therefore, it is useful to develop a repeatable methodology for preparing Corona imagery in these environments. In doing so, a historic mosaic can serve as both a qualitative source of information for characterizing the landscape and as the basis for further exploratory analysis using novel approaches for deriving land cover information. There is also an opportunity to explore new methods for extending the use of Corona imagery to quantitative assessments.

Deriving quantitative information about the spatial extent and arrangement of dune types, grassland and vegetation cover, and the extent of built-up areas, cropland, and pastures will allow for an assessment of how these cover types have changed over time. Given that Corona imagery contains no spectral information, it is impossible to utilize the dominant spectral approaches for deriving land cover information and assessing degradation. This provides an opportunity to evaluate the use of a new method of texture analysis, contextual features, for generating quantitative information from Corona imagery to serve as inputs to a classification algorithm. Generating a historic land cover dataset not only enhances our understanding of the extent of various cover types in the 1970s but has the potential to contribute to long-term monitoring assessments by extending the availability of data for detecting change.

This work will:

1. Generate a mosaic of Naiman Banner using Corona imagery. In order to accomplish this objective, it is necessary to accurately georeference Corona imagery, account for geometric and brightness distortions, and mosaic the images.
2. Apply surface texture statistics, contextual features, to the mosaicked Corona imagery in order to generate information for a classifier
3. Create a classified land cover dataset based on the contextual features

Chapter 3: Proposed Methodology for Georeferencing and Mosaicking Historic Corona Imagery in Northern China

3.1 Introduction

Satellite imagery plays a key role in analyzing land cover change and is important for documenting disturbances (Brogaard & Prieler, 1998; Li et al., 2015; Song et al., 2015; Xu et al., 2018), assessing the impact of policy decisions (Li et al., 2017; Zhang et al., 2012), and predicting the future health and structure of landscapes over time. However, the regular acquisition of moderate resolution satellite imagery did not begin until 1972 with the launch of Landsat 1. Thus, much of the work surrounding land cover change only extends back to that time and we have much less understanding about landscapes prior to this, particularly outside of the United States. In the absence of repeated satellite data, other sources of land cover information, such as historic maps, aerial photography and field data can be used to derive additional timepoints of data and establish baseline conditions for comparison to contemporary data. However, aerial photography must be digitized, and is not always available, particularly outside of the U.S.

One such source of historic imagery is Corona imagery, which is high spatial resolution satellite imagery collected worldwide by the United States in the 1960s and 1970s. However, Corona imagery remains underutilized due to the challenges associated with preparing it for use. The imagery contains no spatial reference information and must be georeferenced. Additionally, inherent distortions from the acquisition process must be corrected before the imagery can be analyzed. Many regions have changed significantly since the acquisition of Corona imagery or contain very few persistent ground features,

often making this process difficult and time consuming. In particular, locating a sufficient number of ground features in very rural areas such as Naiman Banner presents a challenge, particularly when ground features are either too small in scale to detect with moderate resolution reference imagery, or are not evenly distributed throughout the landscape. Very few studies which have utilized Corona imagery detail the georeferencing process in enough detail to replicate. The purpose of this project is to demonstrate a workflow for georeferencing Corona images that can be used by researchers working in highly dynamic landscapes with little to no reference data. Here I document the approach I took to pre-process Corona imagery for a region of northern China that has undergone significant modification since the 1960s. The final product can be used in future research to provide a set of data on landscape conditions that predates anything available at this time.

3.1.1 Corona Missions

The Corona program consisted of 144 reconnaissance satellites produced and operated by the National Reconnaissance Office from June 1959 to May 1972 in order to gain military intelligence during the Cold War. Single-band panchromatic images were acquired worldwide with particularly focus on political hotspots like the Soviet Union, China, and the Middle East at spatial resolutions varying from 1.8 meters to 12.2 meters (Earth Resources Observation and Science Center, 2018) Figure 4 shows the coverage of the Corona missions and imagery hotspots. The photographs were acquired on film via satellite and later scanned to 8-bit panchromatic images (National Reconnaissance Office, n.d.)

Figure 4

Corona Imagery Global Coverage (1962-1972)

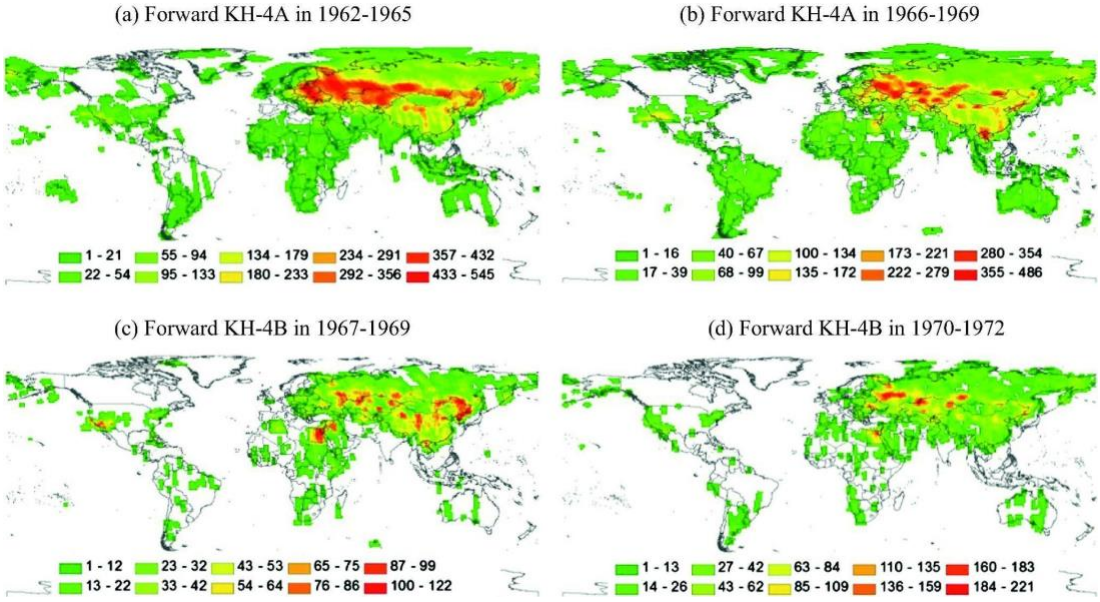

Note. This image depicts the coverage of Corona images acquired by the forward-looking cameras during the KH-4A and KH-4B missions (Song et al., 2015)

During each mission, the imaging satellite orbited around the earth several times, acquiring photographs that cover approximately 13.8 km by 188 km on the ground (2,595 square km in area) (Song et al., 2015). Later satellites were equipped with two panchromatic cameras, one forward and the other backwards (aft) at 15 degrees off-nadir in either direction, with the aft camera roughly six frames behind the front camera (Fowler, 2006). Because of this dual-angle system it is also possible to utilize both camera angles to model topography in the landscape and generate digital elevation models (Casana & Cothren, 2008, 2013; Sohn et al., 2004). The final camera design, KH-4B, is widely considered to be the most useful for modern analysis because of the high quality of the imagery (Sohn et al., 2004). The KH-4B camera operated over seventeen missions between September of 1967 to May of 1972 and returned images with an

approximate ground resolution of 1.8 meters (six feet) at nadir (National Reconnaissance Office, n.d.).

The images taken by the Corona satellites remained classified as top secret until 1992. In 1995, President Bill Clinton signed an executive order declassifying over 800,000 images. High performance film scanners are used to digitize the film at 1800 dots per inch (dpi) and are accessible to the public through the United States Geological Survey's Earth Explorer (Earth Resources Observation and Science Center, 2018).

3.1.2 Georeferencing Corona Imagery

Corona images acquired from the USGS have no spatial reference. This means that the images lack the necessary geo-corrections required to display them over their real-world location using mapping software. In some applications, high geo-location accuracy may only have minor implications for interpreting the imagery, such as when only visual interpretation is required. However, in order to utilize Corona imagery in location-specific analysis such as time series and change detection analyses, it is important to accurately georeference the imagery because mismatches in pixel alignment will result in missing or false detection of change. In such cases, the level of accuracy required to use the georeferenced Corona imagery will depend on the spatial resolution of the other datasets in the analysis (Song et al., 2015). Georeferencing Corona imagery is useful outside of land cover change analyses as well and has frequently been used in identifying archeological features (Casana & Cothren, 2008; Goossens et al., 2006; Ur, 2007).

Accurate georeferencing of Corona imagery is difficult due to the challenges presented when overlaying scanned photo strips on real-world terrain. In addition to

several types of geometric and brightness distortions present in the imagery from the acquisition, the flattened images do not account for varying topography (Hamandawana et al., 2007; Sohn et al., 2004). Several studies have analyzed and proposed methodologies to account for the distortions present in the imagery from acquisition (Hamandawana et al., 2007; Sohn et al., 2004; Zhang et al., 2020). Multiple studies involving Corona imagery detail a similar approach to georeferencing which utilizes ground control points from nearest-date Landsat MSS or TM imagery at the nearest future date to co-register the image (Saleem et al., 2018; Shahtahmassebi et al., 2017; Song et al., 2015; Zhang et al., 2020). Zhang et al. utilized recent high-resolution Google imagery to help identify stable ground features such as road intersections in Corona and Landsat MSS imagery (2020). While most studies opt for remote sensing software for georeferencing, such as ERDAS Imagine, a few utilize a structure-from-motion photogrammetry method of georeferencing (Munteanu et al., 2020; Nita et al., 2018). Almost all studies focus on imagery collected during sixteen missions between 1967 and 1972 using the KH-4B sensor due to its high spatial resolution (1.8 meters) and high image quality. Some Corona imagery that has been previously orthorectified (georeferenced and corrected using a digital elevation model) is available to the public for download as NIFT files through the University of Arkansas' Center for Advanced Spatial Technology's Corona Atlas, though it is worth noting that some of the imagery has been automatically orthorectified and therefore the accuracy is not guaranteed (Center for Advanced Spatial Technologies, University of Arkansas & United States Geological Survey, n.d.).

Despite the increasing number of studies that make use of Corona imagery and efforts to make it widely available for use, few studies provide a set of reproducible methods or steps for georeferencing. Studies that have presented methodology in enough detail to replicate are now dated and must be adapted to modern datasets and methods (Hamandawana et al., 2007; Rigina, 2003). Further, most work has been focused on urban and agricultural landscapes, with persistent features that can be utilized to generate ground control points. It is still unclear how well Corona can be utilized in arid and semi-arid environments which are highly variable in cover and topography. This study presents a workflow for georeferencing Corona images in greater-than-average detail using ArcGIS Pro, a common and readily available software system, that others can easily replicate with the goal of reducing the time and training required to prepare Corona imagery and ultimately expand its use across many disciplines.

3.2 Study Area

The focal area for this study is the central portion of Naiman Banner, located in the eastern portion of Inner Mongolia about 700 kilometers northeast of Beijing in the Horqin Sandy Lands. A detailed history of the study area, it's location and current conditions is available in chapter two of this thesis.

3.3 Objectives

The main objective of this chapter was to georeference Corona imagery within an acceptable range of accuracy in order to generate a mosaic for Naiman Banner, Inner Mongolia. In addition to exploring the applicability of various georeferencing techniques within the context of a semi-arid, and variable landscape, the historic mosaic will serve as the basis for an exploratory contextual features-based classification analysis in the

following chapter. Georeferencing and analyzing the historic mosaic also contributes to the overarching objective of this thesis which aims to explore historic landscape conditions and land cover types in Naiman Banner in the late 1960's and early 1970's.

3.4 Data Collection

3.4.1 Corona Images

Corona images were obtained from the USGS's Earth Explorer. Only images from the KH-4B system were considered since missions using the dual-camera system have the highest spatial resolutions. This includes missions 1101 through 1117 (excluding mission 1113, which failed). Images were filtered to contain less than 20% cloud coverage and intersect with the bounding coordinates of the study area. It is important to note that since the images are unreferenced, USGS approximates the location of Corona images when displaying them in Earth Explorer. Some images that overlapped with the bounding coordinates within Earth Explorer's search criteria did not intersect with the study area when positioned manually in mapping software. Priority was placed on finding images with the fewest visible errors. Scan lines, bright/dark spots, and blur spots were amongst the most commonly found errors. In addition, priority was placed on images where the study area was positioned in the center of the image rather than needing to mosaic multiple images along their vertical edges. This is because greater distortions occur towards the edges of Corona images, and this would require mosaicking along a greater number of seams. When possible, all images should also be acquired on the same date to avoid differences in image quality. And lastly, all images should be acquired from the same camera direction, forward or aft (backwards). For purposes of this study, either direction would have been sufficient. The dual directions have been utilized to generate

digital elevation models (Casana & Cothren, 2013), however, this is not useful in this case given the high variability and frequent movement of the dunefields in Naiman Banner.

Four images, captured on November 30, 1970, were acquired based on the criteria described above. The images were captured during mission 1112 from the aft camera. Additional details about this mission can be found in Table 1 and the Corona image IDs can be found in Table 2. Henceforth, unreferenced images will be referred to as strips. Figure 3 shows the position of the four unreferenced strips in relation to the study area.

Table 1

Mission Details of Acquired Corona Imagery

Image Collection Date	November 30, 1970
Mission Number	1112
Camera Type	KH-4B (dual camera)
Camera Resolution	Stereo High
Ground Resolution (at Nadir)	~1.8 meters
Camera Type	Aft (backward facing)
Direction Flag (Direction of Acquisition)	183D
Revolution	D

Table 2

Corona Images Acquired for Georeferencing of Naiman Banner

Image Number (from North to South)	Corona Image ID
1	DS1112-2183DA070
2	DS1112-2183DA071
3	DS1112-2183DA072
4	DS1112-2183DA073

3.4.2 Other Imagery

Landsat Thematic Mapper (TM) and modern high spatial resolution basemap imagery from ESRI were used for locating stable ground control points. A cloud-free Collection 1 Tier 1 Landsat TM image captured by Landsat 5 was acquired from USGS' Earth Explorer. The closest data available to that of the Corona images was taken on December 8, 1984. It is helpful to have an older reference image in landscapes where ground features have changed dramatically between the collection of the Corona imagery and contemporary imagery. Contemporary imagery was acquired from ESRI for the year 2019. Figure 5 shows both reference imagery datasets in relation to the study area.

Figure 5

Landsat TM Imagery (1984) and Contemporary Imagery (2019)

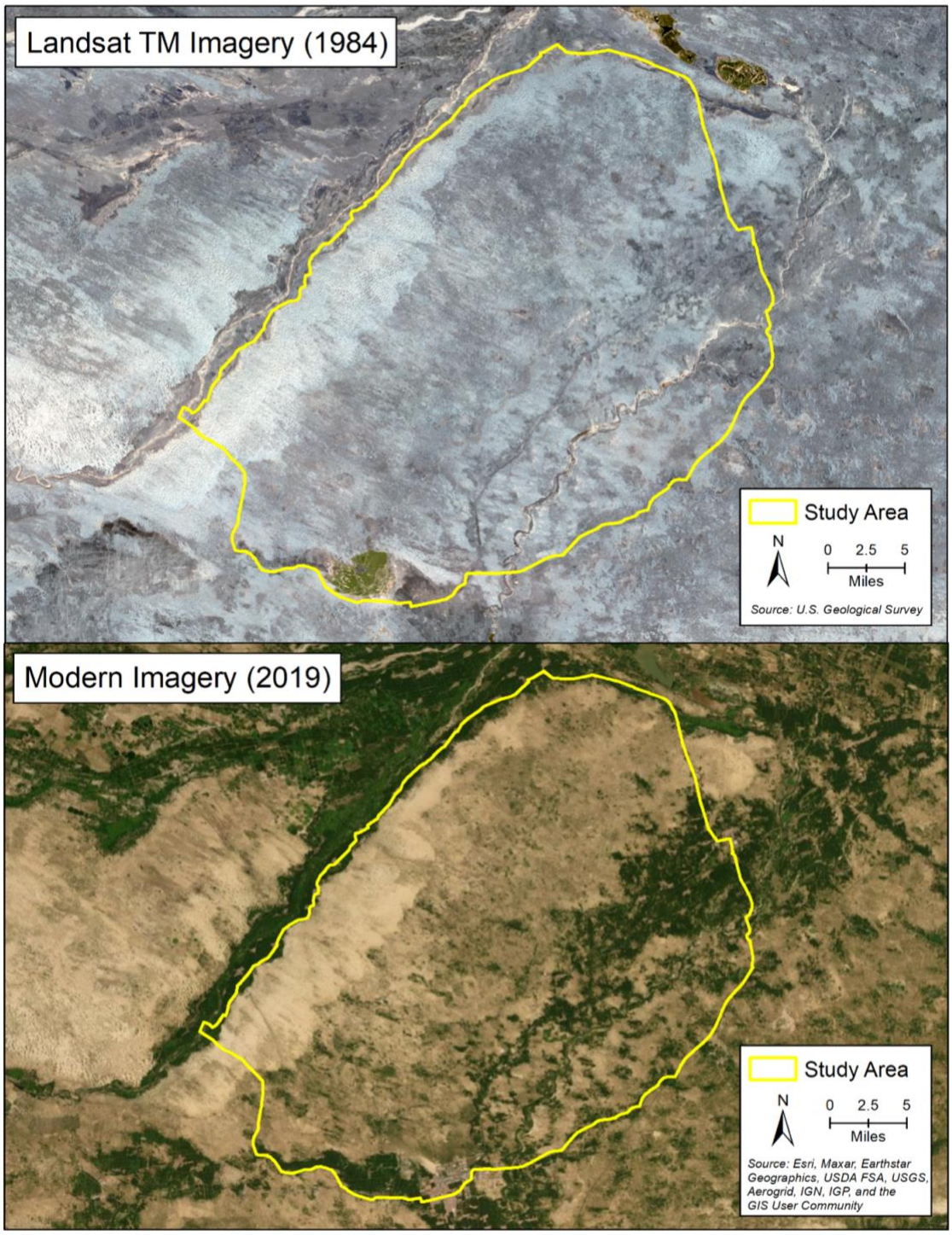

Note. Landsat TM imagery was acquired on December 8, 1984 from USGS and contemporary imagery was produced by ESRI in 2019. These images were used as reference datasets for georeferencing Corona strips

3.5 Methods

3.5.1 Preprocessing

Several preprocessing steps are required to prepare Corona imagery for georeferencing. Each strip is delivered in four separate files which, when combined, represent one Corona acquisition during the mission. Strip parts are delivered at a 180-degree rotation. Additionally, each Corona strip contains a black film border which must be trimmed before georeferencing (Rigina, 2003). Figure 6 details a workflow for the entire georeferencing process.

The four files for each strip, referred to in this paper as parts A through D (from left to right), should be mosaicked into a single strip prior to georeferencing in order to maintain consistency across the strip. There is about six kilometers of overlapping area between strip parts (Figure 7). Because strip parts are only segmented due to file size, not due to differences in image acquisition, the parts should fit together near-perfectly. Since the objective is simply to join the parts back together, the mosaic operator (which defines how overlapping pixels in the mosaic are resolved) should be defined using a first or last method rather than an averaging method.

After trials on several platforms, it was determined that ArcGIS Pro's georeferencing interface was the most efficient software for georeferencing Corona imagery. Here, version 2.8 of ArcGIS Pro was utilized. ArcGIS Pro allows the user to move, scale, and rotate the unreferenced strips over other image datasets and toggle between images quickly when placing ground control points. Additionally, the impact of ground control points on the reference are visible immediately as you select them, allowing the ability to gauge the quality of each point.

Figure 6

Recommended Workflow for Georeferencing Corona Imagery

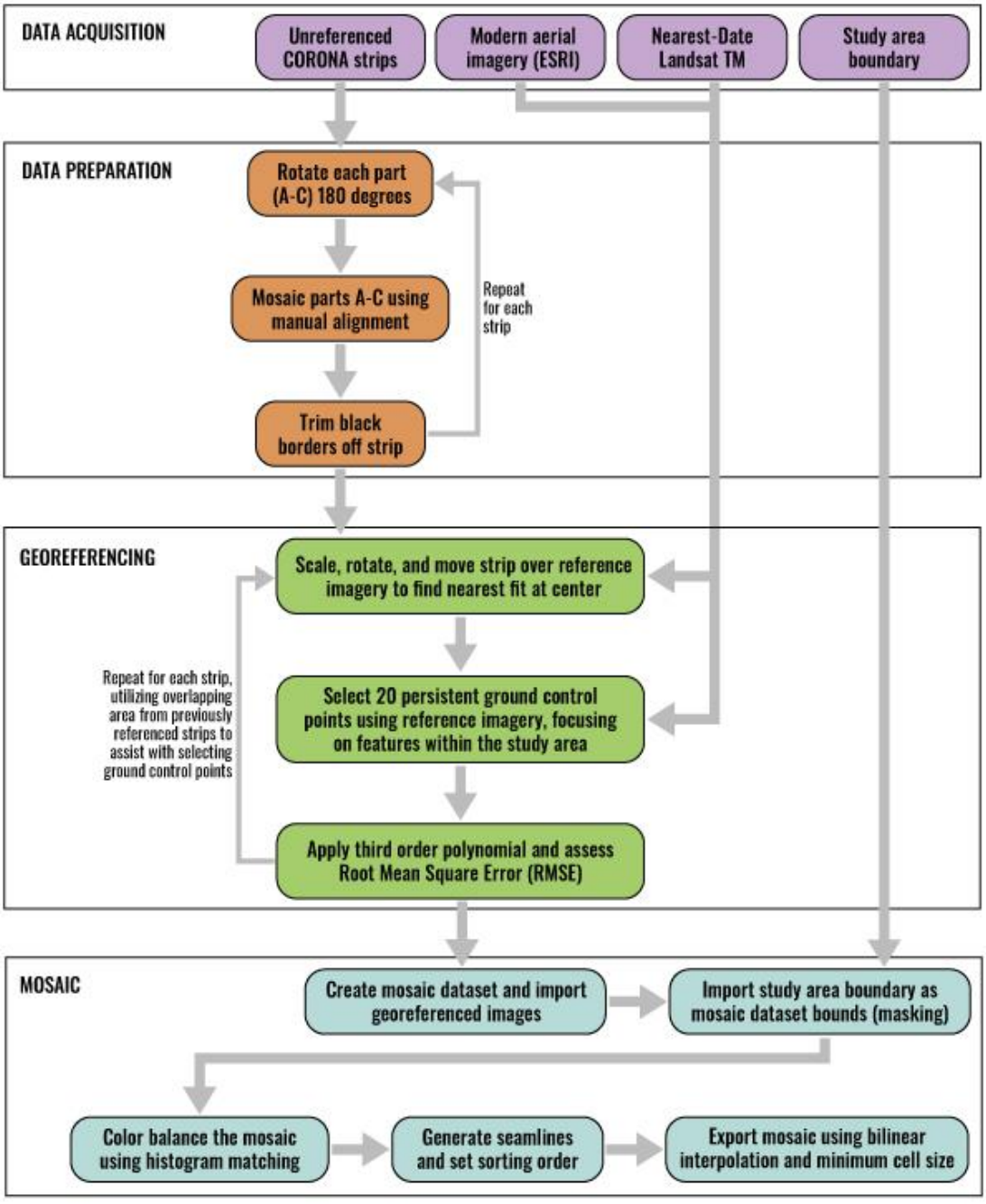

Parts A through C of each strip were scaled and rotated over contemporary imagery to approximate their location. The exact location of each strip can be further refined once the parts are mosaiced together. Spatial reference is not required to mosaic

the strip parts, but the underlying imagery may be helpful for determining their relative overlap. Part D of each strip was located beyond the bounds of the study area and was therefore excluded from the mosaic. However, it is important to note that there should be a suitable buffer of imagery surrounding the desired study area in order to account for warped edges caused by georeferencing. If the study area boundary lies close to the edge of the strip, additional pieces from surrounding strips should be included in the georeferencing process. Figure 7 shows the location of the study area with respect to parts A through C across the four strips.

After mosaicking, the boundaries of the four strips (excluding the black film borders) were each traced manually to produce a clipping geometry for trimming the borders away. It is important to trim the borders prior to georeferencing in order to properly visualize the alignment of the overlapping areas between strips (Rigina, 2003). Finally, the location of each strip was further refined over the reference imagery.

Figure 7

Strip Diagram

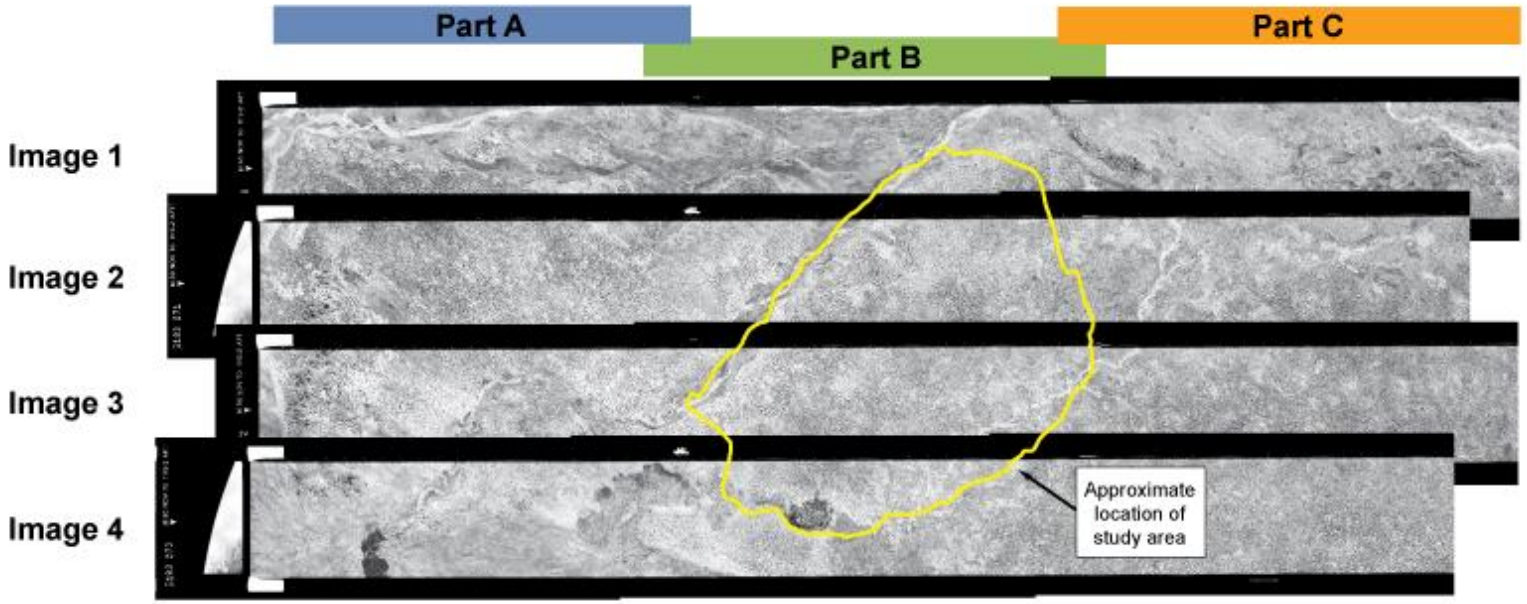

Note. Approximate location of the study area across four unreferenced and untrimmed Corona strips. Notice that each part of the strip (A-C) overlaps. The overlapping area, prior to georeferencing, measures approximately six kilometers.

3.5.2 Georeferencing

Once each Corona strip is positioned as accurately as possible over the reference imagery (accounting for distortions which will prevent ground features from perfectly aligning), ground control points were used to refine the spatial reference. Each Corona strip should be georeferenced individually rather than as a final mosaic. This will result in a more accurate mosaic since the georeferencing transformations can account for unique distortions in each strip.

When possible, it is advised to begin the georeferencing process on the strip with the largest number of potential quality ground control points, particularly where the largest number of persistent structures or roadways exist. Once this strip is georeferenced it can be used as reference imagery for other overlapping, unreferenced strips. While not a typical approach for georeferencing in remote sensing, Hamandawana et al. (2007) proposed this methodology for Corona imagery because of the unique challenges associated with detecting a sufficient number of quality ground control points in many Corona scenes. They recommend georeferencing a "primary" strip and then, if necessary due to a lack of quality ground control points in the overlapping strip, match features in the referenced Corona strip to features in the unreferenced strip within the area that they overlap (Hamandawana et al., 2007). For this study area, the most practical primary strip to build from was image four (the southernmost image) because there are significantly more persistent features which could serve as ground control points, including the present-day city of Naiman. Subsequent images were georeferenced using Hamandawana et al.'s approach, moving from image four to image one in reverse chronological order

and making use of the overlapping area with the previously referenced image when necessary (2007).

Based on reports from previous studies (Casana & Cothren, 2013; Gurjar & Tare, 2019; Nita et al., 2018), it was determined that at least 20 ground control points should be collected for each strip for a total of 80 ground control points across four strips. A minimum of 10 ground control points is required to georeference with a third order polynomial (Environmental Systems Research Institute, 2018). Distinct features such as built-up urban areas and road intersections are best for georeferencing because they are typically static through time. Corona imagery presents a unique challenge in that a majority of useful features for ground control points did not exist in this area in 1970. Additionally, utilizing Landsat TM imagery as a reference point is difficult because of its lower spatial resolution. Many of the built-up areas and road crossings present in Naiman Banner in 1970 are not visible in the Landsat TM imagery and therefore cannot reliably be referenced to the Corona imagery. Modern imagery is also difficult to utilize due to the dynamic and changing landscape in Naiman Banner, with shifting dunes and rapidly expanding urban areas. Locating reliable ground control points was time consuming and required a combination of both reference imagery and making use of overlapping, previously georeferenced strips. Examples of ground control points using several imagery dates can be seen in Figure 8.

Figure 8

Ground Control Points Shown Between Corona, Landsat TM, and Contemporary Imagery

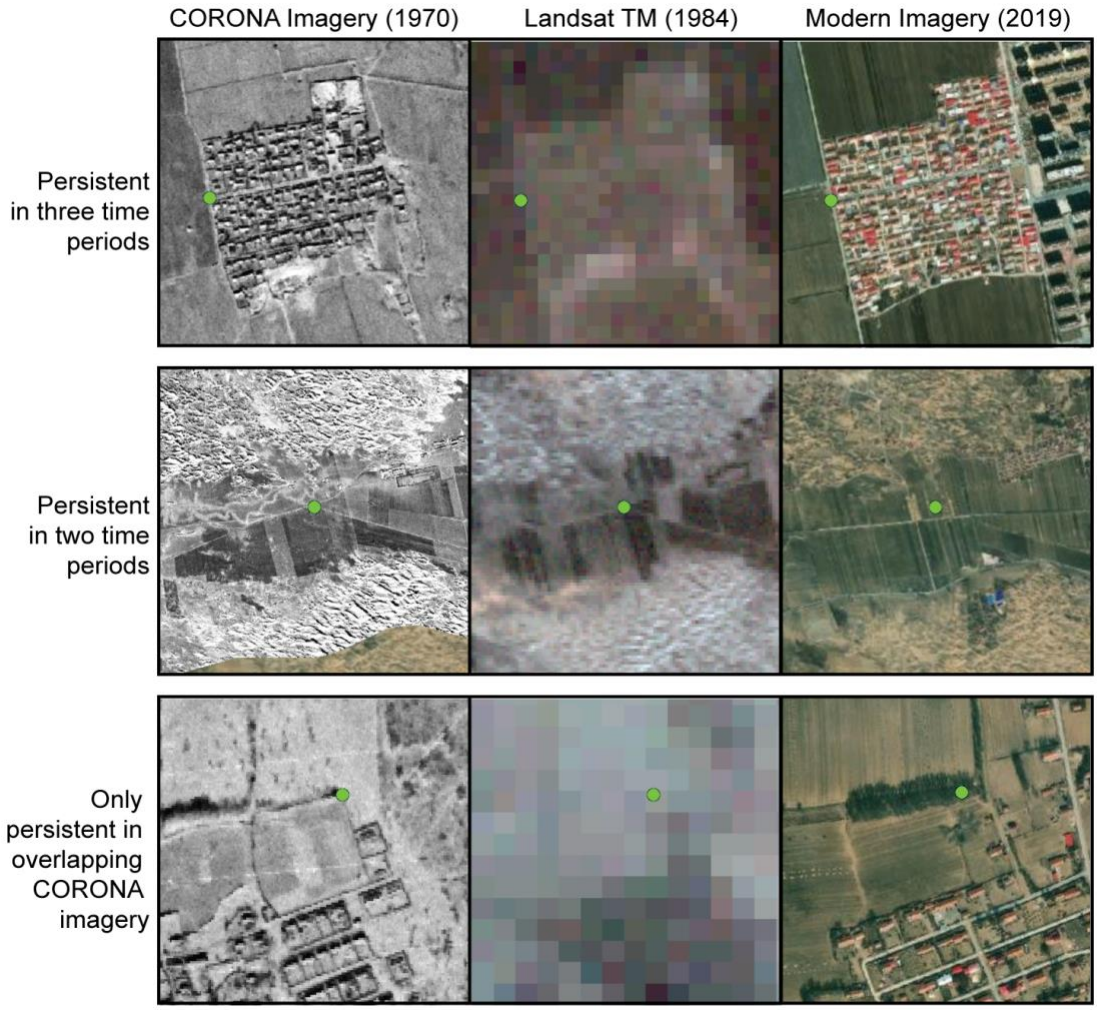

Note. Some ground control points were persistent in all three sets of imagery, while others could only be detected in either the Landsat TM or contemporary imagery. Some ground control points could not be detected in either, but were selected using persistent locations in overlapping areas between Corona strips

Ground control points were categorized into one of four types: roadways, overlapping areas, structures, and natural features. Roadways, which consisted predominantly of intersections in small built-up areas that have grown into larger settlements since the acquisition of Corona imagery, accounted for 52.5% of all ground

control points. In some instances, informal path networks connecting settlements and grazing areas were also useful. Overlapping strip features accounted for 18.75% of ground control points. These features generally consisted of distinct natural edges. While it is not recommended to utilize natural features such as bodies of water or sand dunes as ground control points because it is less certain that the features have not shifted position between image dates, it is acceptable in this case because the natural features are selected using other Corona images that were acquired at the same time. While this type of ground control point should be used sparingly since they rely on the accuracy of the previously referenced strip, it was impossible to find enough persistent ground control points throughout the four strips to avoid them entirely. Similarly, natural features in non-overlapping areas should be used sparingly because they are less reliable given that natural features such as dunes and bodies of water vary over time. Natural features accounted for 13.75% of ground control points in this study and primarily consisted of persistent cropland edges. Structures accounted for the remaining 13.75% of ground control points. This consisted predominantly of building corners and one persistent grazing enclosure. The sum of each type of ground control points can be found in Table 3.

Table 3

Types of Ground Control Points Collected

Type of Ground Control Point	**Number of Ground Control Points**
Roadways (paved and unpaved roads, paths, and trails, predominantly at intersections)	**42**
Overlapping Strip Feature (distinct natural features such as bodies of water or dune edges)	**15**
Natural Features (distinct naturally occurring objects like rock formations or corners of persistent agriculture fields)	**11**
Structures (building corners, fencing enclosures)	**11**
TOTAL	**80**

Focus was placed on selecting ground control points within and closely surrounding the study area. When ground control points were selected evenly throughout the strips, including the corners and edges of the images, the overall accuracy of the georeferencing decreased. This is because distortions are greater towards the edges of the strips and the polynomial must compromise accuracy to fit to these distortions. Since the study area was centrally located in the strips and the edges would be removed, we decided to place ground control points in such a way that would overly warp and compromise the far edges of the strips in exchange for greater accuracy within the study area. However, some points had to be placed outside of the study area to anchor it so that warping did not occur within the boundaries. The location of the final ground control points throughout the strips can be found in Figure 9.

Figure 9

Location of Ground Control Points

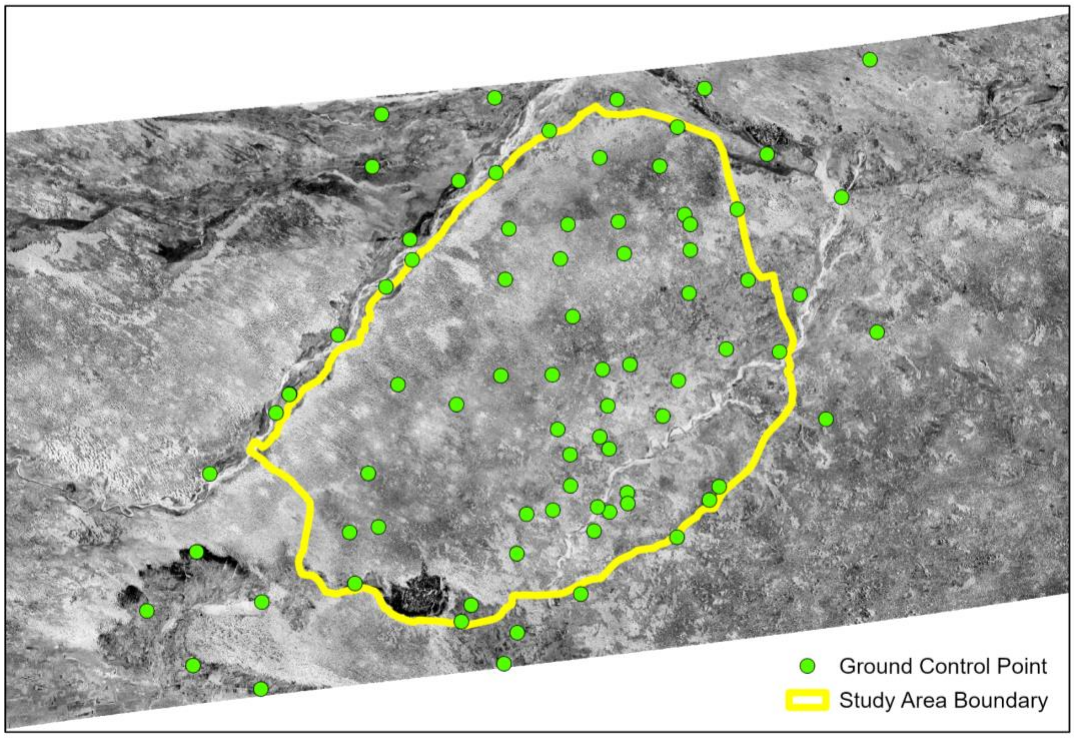

Note. 20 ground control points were collected for each Corona strip for a total of 80 ground control points. Ground control points were selected in and closely surrounding the study area, which compromised and overly warped the strips beyond the bounds in exchange for greater accuracy within it.

A third order polynomial transformation was applied to each strip to fit the ground control points. A second or third order polynomial transformation is recommended when there are significant distortions in the imagery because the strip can be bent and curved rather than just shifted, rotated, and scaled (Figure 10) (Environmental Systems Research Institute, 2018). However, as mentioned previously, it is important to anchor strip edges within the study area when using a higher order polynomial because extreme edge warping may result in gaps between strips.

Figure 10

Georeferencing Polynomials

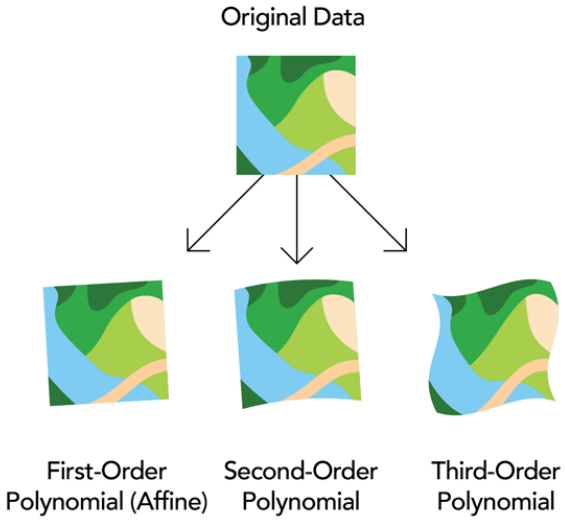

Note. Example of first, second, and third-order polynomials on an image (Environmental Systems Research Institute, 2018)

3.5.3 Mosaicking Georeferenced Strips

Once each Corona strip was georeferenced within the acceptable measure of accuracy (<15m), the images were combined using ArcGIS Pro's Mosaic Dataset tool. Mosaic datasets are used within ESRI software to manage, analyze, and display multiple rasters as one dataset, accompanied by a suite of tools to enhance the mosaic such as color balancing and generating seamlines. First, the four georeferenced images were imported into an empty mosaic dataset. A shapefile with the boundary of the study area was imported into the mosaic dataset as the boundary parameter. The boundary was then applied as a mask to the mosaic, removing the edges of the images that fell outside of the study area. This eliminates the need to clip the mosaic later during export, which I found saved computational power.

Next, brightness variations were accounted for using color balancing techniques. Color balancing the mosaic is important because the range of digital numbers (DNs) in

each strip can vary, impacting both the appearance and statistics of the final mosaic. Edge darkening and blurring is noted to occur increasing towards the outer edges, likely due to the oblique angle of the camera for features distant from nadir, and other bright and dark spots may occur due to changes in sun angle (Hamandawana et al., 2007). However, since high-quality images that contained minimal spotty distortions were chosen, and because the edges were being clipping away from the study area, no major distortions needed to be accounted for.

In addition to a smoother visual output, color balancing ensures that the distribution of pixel values is consistent across the mosaic. This is crucial for later analyses where pixel values are used to derive features, such as the contextual feature analysis described in chapter four. Color balancing applies an algorithm that manipulates pixel values across several images to equalize them to one another. I chose to apply a histogram match based on a visual inspection of outputs using different balancing techniques. A histogram match changes each pixel's value according to its relationship with a histogram composed of all of the input images or the histogram of one target input image (Liu et al., 2011). This approach is recommended when all of the images have similar histograms and features are generally consistent throughout the images, which was the case for this study area. Since the images in this study did not contain inconsistent coloring that would need to be corrected manually, a uniform color balancing approach for the entire mosaic was appropriate. However, where uneven bright or dark spots occur, Hamawanda et al. propose several methodologies for accounting for them (Hamandawana et al., 2007).

Next, seamlines were generated for the mosaic dataset. Seamlines are used to sort overlapping imagery and produce a smoother transition between images. Computational methods for generating seamlines use either overlapping geometries of the images or the spectral characteristics of overlapping areas. Through experimentation, I found that generating seamlines based on the physical footprint of each image produced the smoothest result, whereas utilizing a radiometric approach is not useful due to lack of spectral information. Once seamlines were generated, I inspected the mosaic using different image overlaps in order to determine an order that produced the smoothest seams. An overlap ranking field was created and populated in the mosaic dataset's attribute table to assign the image order and the sort method for the mosaic was defined by this attribute. The overlap method was set to "first " which assigns the final pixel value of the mosaic to the higher-ranking image in overlapping areas. A blend or feathering method, which averages the values of two overlapping pixels, distorted features found along overlapping areas and should therefore be avoided.

3.5.4 Exporting the Mosaic

During the georeferencing process, individual cells are skewed in both shape and size and must be resampled back to a standardized grid format for use in other analyses (Figure 11). Cell sizes varied in both height and width for each strip (Table 4). The minimum cell size of 2.5 meters and a bilinear interpolation sampling method were used for resampling. The nearest neighbor interpolation method resulted in a blockier final product and should therefore be avoided unless computational power is a concern. A script which documents the workflow used to mosaic and export georeferenced Corona images in Python can be found on GitHub.

Figure 11

Skewed Cells After Georeferencing

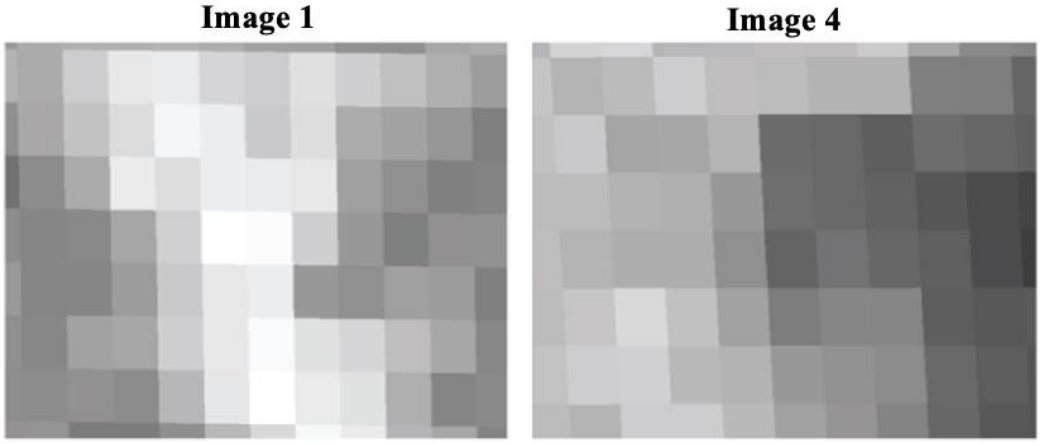

Note. Difference in cell size and shape between image one (left) and image four (right) after georeferencing

Table 4

Cell Size of Images After Georeferencing

Image #	Cell Size X	Cell Size Y
1	2.500	3.911
2	2.677	4.334
3	2.564	3.858
4	2.662	4.432

3.6 Assessment of Final Mosaic

The final georeferenced mosaic has a spatial resolution of 2.5 meters and is shown in Figure 12. The average Root Mean Square Error (RMSE) for the mosaic was 11.77 meters, with RMSE values for each of the four images ranging from 9.17 meters to 14.22 meters (Table 5, Table 6). This aligns with accuracy values achieved throughout the literature for georeferencing Corona imagery, which is less than 15 meters in most cases (Casana & Cothren, 2013; Gurjar & Tare, 2019; Nita et al., 2018; Shahtahmassebi et al.,

2017). I hypothesize that the reason that image four has the highest accuracy amongst the four images is because this image was georeferenced first and contained the highest number of persistent ground control points that were either roadways or buildings. Since the subsequent images contained fewer settlements and therefore fewer potential ground control points, they each contain several ground control points that make use of the overlapping area between the previously georeferenced image. This is likely the cause of slightly lower accuracy for images two, three, and four.

Table 5

Mean Accuracy of Final Corona Mosaic

Mean Forward Accuracy (meters)	11.775
Mean Inverse Accuracy (pixels)	12.619
Mean Forward-Inverse Accuracy	3.477

Table 6

Accuracy of Corona Strips in Final Mosaic

Image #	Number of Ground Control Points	Forward Accuracy (meters)	Inverse Accuracy (pixels)	Forward-Inverse Accuracy
1	20	11.751	13.352	2.177
2	20	13.710	13.710	1.434
3	20	14.239	14.223	2.725
4	20	9.173	9.173	3.477

Figure 12

Final Mosaic of Naiman Banner, Inner Mongolia

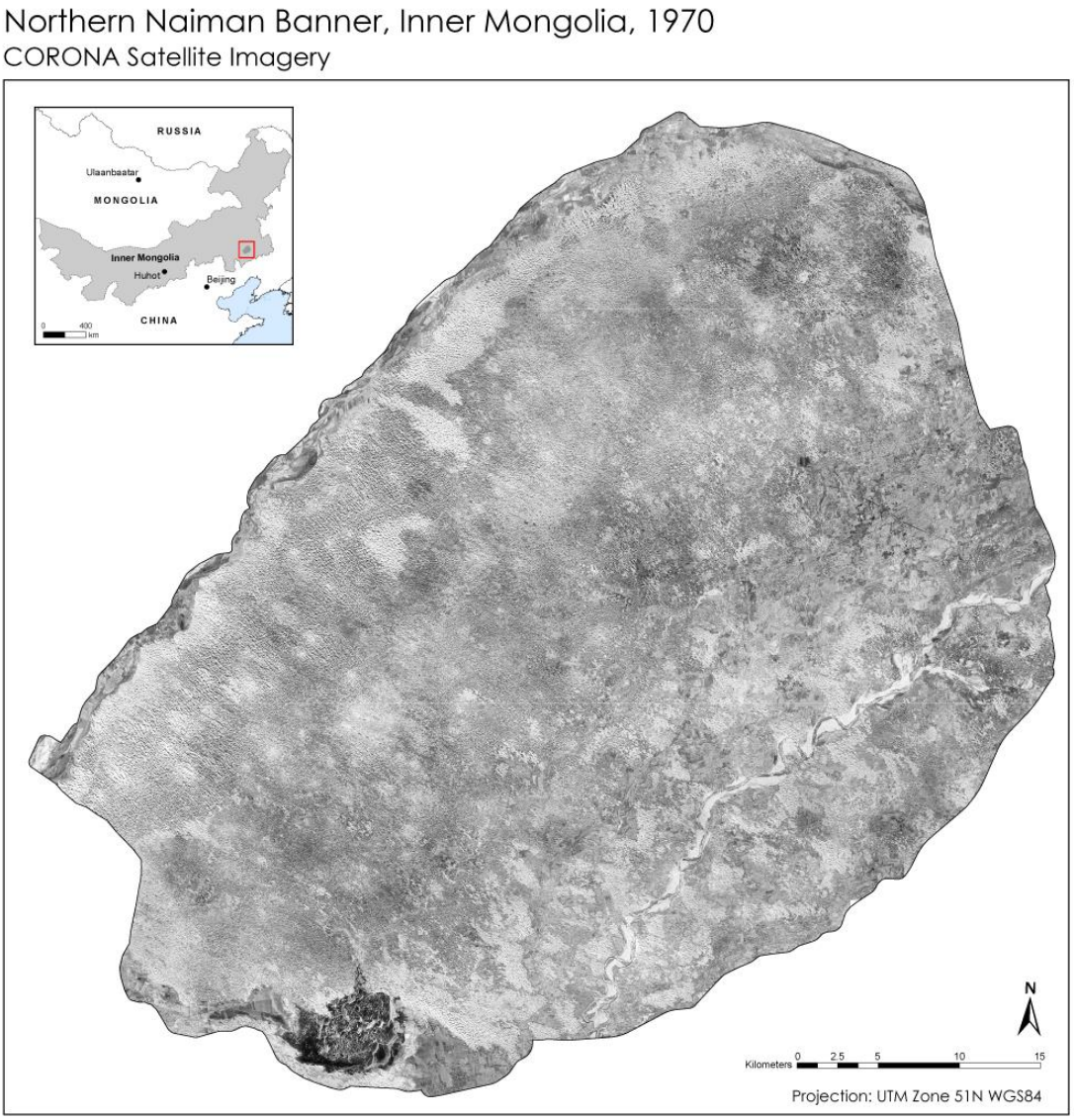

Note. The final mosaic consists of four georeferenced Corona images and has an overall accuracy of 11.77 meters.

The mosaic contains very few visible seam lines and the transition between images is smooth. However, upon utilizing the Corona mosaic in a land cover classification (described further in chapter four), it was discovered that, despite utilizing a histogram matching approach to match the range of pixel values across the four images,

there were some persistent differences in pixel values between images. This was not immediately apparent because the mosaic looked visually smooth after applying the color balancing techniques. However, the pixel values of image 1 (the northmost image) still differed from the pixel values of the other images for equivalent features in the landscape. This is likely due to the fact that the range of values in image one represented a narrower range of features, and those features had more extreme values on both ends of the pixel range. For example, mobile dunes had brighter, higher value pixels in this image than in the other images, and vegetation had darker, lower values. Differing pixel values between the images impacted the output of the classification in such a way that land cover types on either side of the seamline were classified into separate clusters, and it is clear that a histogram matching approach was not sufficient to account for the extreme range represented in image one. A methodology for accounting for color balancing issues that are discovered downstream in the analysis is detailed further in chapter four of this thesis. However, it is recommended to thoroughly assess the underlying statistics of each image in the mosaic as well as in the resulting color balanced mosaic in order to avoid this. This is particularly important when the pixel values of the mosaic will be utilized to generate new information. In applications where the objective is simply to achieve a smooth visual output, a simple color balancing approach such as the one described in the methodology should be sufficient.

3.7 Discussion

3.7.1 Evaluating the Methods

Despite the challenges associated with using Corona imagery, this study demonstrates a methodology for successfully georeferencing Corona imagery at a high

level of accuracy. Working with Corona imagery is time-consuming primarily because the literature surrounding their use lacks any robust or repeatable workflows that would streamline the process and reduce unnecessary experimentation. This study demonstrates a tractable and replicable workflow for georeferencing Corona imagery at a high level of accuracy using a singular platform— ArcGIS Pro—which is widely available and commonly used. This broadens the applicability of the workflow to a wider range of researchers and reduces the learning curve, and therefore labor for those interested in utilizing Corona imagery.

While these methods were developed intentionally to be highly replicable, they should be adapted according to the unique requirements of both the imagery and the scene. The area of interest in this study was located centrally across four strips and did not include any of the intense color distortions found in some Corona images. For study areas that span the edges of Corona images and/or require mosaicking along vertical edges, accuracy of the final mosaic may decrease due to the greater distortions found along edges (parts A and D). Additional research into the specific shape and scale of distortions near edges is needed to adapt the methodology accordingly.

Additionally, unique color distortions such as brightness, dark, or blurred spots may require advanced color balancing techniques not described in this paper. Similarly, some landscapes may possess even fewer persistent ground features, such as areas where no settlements or road networks exist. In these instances, I recommend reducing the number of ground control points from twenty to ten (the minimum required to utilize a third order polynomial), or six with a second order polynomial. This will likely reduce

the accuracy. For landscapes similar to the study area described here, the methods detailed in this paper should prove adequate for highly accurate georeferencing.

It is difficult to imagine a fully automated script for georeferencing Corona images given the complex and varying nature of distortions within the imagery and in different landscapes. However, this study has demonstrated that the georeferencing process can be accomplished entirely within ArcGIS Pro using python-based tools. Therefore, as demonstrated in the mosaicking process executed using a python script, there are opportunities to automate portions of the process and create user-facing toolboxes or applications. This would reduce the technical training required to georeference and, in turn, increase accessibility to research in other disciplines.

3.7.2 Initial Assessment of Landscape Changes

In addition to a detailed and replicable methodology, this study produced a mosaic of Naiman Banner, Inner Mongolia in 1970. Historical imagery of land cover in Naiman from this period are sparse. Based on a visual inspection of the mosaic compared to modern imagery, it is clear that the landscape has undergone significant change since the acquisition of Corona imagery. For example, built-up settlements and cropland have vastly expanded while vegetated dunes have decreased and mobile dunes, which are not rooted by vegetation and are often a result of desertification, have increased. Chapter four of this thesis describes a methodology for quantifying land cover in the mosaic, allowing us to further analyze and describe these changes. However, with just the mosaic alone, our understanding of the distribution of different landscape features, including dunes, water bodies and vegetated areas during this time has increased significantly.

3.7.3 Potential Uses of Corona Imagery

Georeferenced Corona imagery is useful in a wide variety of applications. It presents a unique opportunity to detail and quantify historic land cover and extend the timeline of available data for analyzing anthropogenic impacts to landscapes. Due to the high spatial resolution of the imagery, it may also be possible to detail historic landscapes in far greater detail than is currently available, past or present. Chapter four of this thesis utilizes the mosaic output of Naiman Banner to assess the feasibility of utilizing contextual features to derive spatial information and land cover types. The results indicate that the amount and complexity of information that can be derived from Corona imagery is significant and potentially exceeds any other available datasets for Naiman Banner. Generating historic cover types is useful for assessing historic, current and future land use policies and restoration efforts surrounding aeolian desertification in Inner Mongolia.

With highly accurate georeferencing, Corona imagery may also be combined with other image datasets to quantify change at the pixel level. Per-pixel change detection is appropriate depending on the spatial resolution of the other datasets. For mid to high resolution imagery (ten to thirty meters) such as Landsat and Sentinel, which is roughly equivalent to the georeferencing accuracy demonstrated in this study (fourteen meters), measuring per-pixel change is appropriate. Therefore, when classifications methods are consistent across the datasets, Corona imagery can extend the timeline of time series analysis as well. For very high spatial resolution datasets of ten meters or less, such as IKONOS or SPOT imagery, change detection should be used with caution as false

change can be detected where Corona imagery does not align correctly with other datasets.

3.8 Conclusion

Corona imagery presents a unique opportunity to extend the timeline of available information for analyzing changing landscapes. However, Corona imagery remains underutilized due to the challenges associated with preparing them for use and the lack of a robust and replicable methodology in the literature. This study successfully georeferenced four Corona images with a high level of accuracy and describes a repeatable workflow suitable for others to follow. The resulting mosaic of Naiman Banner significantly increased our understanding of the landscape in 1970 and represents one of the first available datasets of its kind. It will also serve as the basis for a land cover classification in chapter four. Corona imagery is an important resource for analyzing long term land use and land cover patterns and their integration in analyses is essential for a broader understanding of anthropogenic impacts to landscapes that continue to drive global environmental change.

Chapter 4: Evaluating the Use of Contextual Features Derived from Corona Imagery To Reconstruct Historic Land Cover Types in Inner Mongolia, China

4.1 Introduction

Desertification and the loss of productive ecosystems due to anthropogenic activity and climate change is regarded as one of the most pressing global environmental issues (Feng et al., 2015; IPBES, 2018; Wang, 2011). The expansion of deserts and degradation of vital ecosystem services provided by grassland systems threatens human livelihood and further contributes to global climate change (International Union for Conservation of Nature, 2017; United Nations Convention to Combat Desertification, 2017). Therefore, it is critical to assess land cover changes in order to document disturbances, assess the impacts of policy decisions aimed at combating and restoring productive ecosystems, and predicting the future health of landscapes.

Satellite imagery has greatly expanded our ability to assess and quantify land cover changes over time, particularly through use of land cover classifications, change detection and time series analyses. However, discrete classifications depicting broad cover types often result in a loss of information. In dynamic & heterogeneous landscapes such as grassland and semi-arid systems, it is often important to understand landscape structure more granularly. This is particularly true for global land cover datasets that are developed for broad applications. Additionally, the regular acquisition of moderate resolution satellite imagery did not begin until 1972 with the launch of Landsat 1, and many assessments do not date back further than the 1980s (Guo & Wen, 2020; J. Li et al., 2015; Wen et al., 2020; Zhou et al., 2015). This limits the timeframe within which we can assess land cover change, and therefore, limits our knowledge of the long-term health and

recovery of landscapes. Due to these data limitations, very little is known about the condition of landscapes in northern China prior to the 1980s, particularly the status and extent of grasslands. Increased cultivation and grazing pressure are documented to have begun around 1978 with the opening of China's economy and intensified further around 1985 through policies such as the Rangeland Law of 1985, meaning the earliest remotely sensed imagery that we have utilized for analysis characterizes already-disturbed landscapes (Robinson et al., 2017; Wang, 2011; Wu et al., 2015). While some level of disturbance is documented before the 1980s (Wang, 2011), extending the timeline of available information still presents an opportunity to better understand the landscape prior to the most intense period of degradation in its history, giving us a better "baseline" understanding of historic conditions. Other sources of land cover information, such as historic thematic maps, aerial photography and field data, are often not available, particularly outside of the US and western Europe. However, where data is available before this timeframe, it represents a huge opportunity to expand our understanding of historic landscape characteristics.

4.1.1 Corona Imagery

Between 1960 and 1972, the United Stated launched a series of classified programs to capture covert images in order to gain military intelligence during the Cold War. The first program, known as Corona, acquired imagery worldwide with particular focus on political hotspots like the Soviet Union, China, and the Middle East at spatial resolutions varying from 1.8m to 12.2m (United States Geological Survey, n.d.). Given the very high spatial resolution for its time, and the fact that these images predate regularly acquired satellite imagery from sources such as Landsat by over a decade,

Corona imagery presents a unique opportunity to analyze land cover and historic landscape conditions in great detail. However, Corona images are 8-bit, panchromatic images, meaning they lack spectral information aside from the gray-tone values used to compose the image. This presents a challenge for conducting a land cover classification because traditional classification approaches rely on segmenting cover types based on the spectral differences found between classes, such as the differing spectral responses of vegetation and urban areas in the near infrared spectrum.

Corona imagery has been utilized in several different ways to assess land cover, including straightforward digitizing of land cover types (Andersen, 2006; Coskun Hepcan, 2013; Franklin et al., 2005; Munteanu et al., 2020; Y. Zhang et al., 2020), object-oriented image segmentation (Gurjar & Tare, 2019; Nita et al., 2018; Rendenieks et al., 2020), and utilizing texture analysis to derive values for a classifier (Gurjar & Tare, 2019; Saleem et al., 2018; Shahtahmassebi et al., 2017; Song et al., 2015). In some cases, approaches were combined—where textures were derived from Corona imagery and the resulting multi-band image served as the basis for an object-based classification (Gurjar & Tare, 2019; Saleem et al., 2018). Song et al. (2015) calculated occurrence textures (data range, variance, mean, entropy, and skewness) and co-occurrence textures (variance, homogeneity, contrast, dissimilarity, entropy, second moment, and correlation) in Corona imagery using various moving window sizes to classify forested vs. non-forested pixels in a machine learning algorithm. Similarly, Shahtahmassebi et al. (2017) used Corona-derived textures in combination with Landsat MSS to derive a continuous land cover classification of forested areas in Fu Yang, China.

Almost all of the literature surrounding the use of Corona imagery for land cover classifications focuses on forested and agricultural landscapes, and predominantly detects the presence or absence of one cover type such as forest or crop fields. Few studies lay out a methodology for classifying land cover types with the objective of better understanding all of the available information in the imagery, and no studies do so for semi-arid and arid landscapes. It is unclear based on the literature if the methods utilized in those studies, particularly the use of texture analysis to extract new information from Corona imagery, would be sufficient for a land cover classification of a highly variable semi-arid landscape. New methods in the field of remote sensing that utilize a more extensive array of contextual texture measures to extract land cover types provides an opportunity to not only test the use of these methods on Corona imagery and semi-arid landscapes, but also to expand the methodology for classifying Corona imagery beyond just binary landscapes.

4.1.2 Contextual Feature Analysis

Contextual features are statistical quantifications of different levels of image feature, such as low level edge patterns, pixel groups, and gaps, which form high level image textures calculated over groups of pixels or neighborhoods (Chao et al., 2021). Spatial feature and texture analysis can help identify patterns and homogeneity in a landscape by analyzing the orientation, geometry, and patterns of pixel groups at various scales. Image metrics such as histogram of oriented gradients (HOG), local edge pattern, and mean are calculated in a kernel (moving window) and reported back at the pixel level (Engstrom et al., 2019). These statistics can provide useful information about the composition and complexity of the landscape at multiple scales, revealing pixel patterns

that often differ between land cover types. While texture analysis has been used extensively for non-spatial image processing, the application to remotely sensed imagery is fairly recent and focuses on urban landscapes with the purpose of detecting built-up human settlements (Engstrom et al., 2019; Graesser et al., 2012; Sandborn & Engstrom, 2016). Therefore, all of the applications of contextual features thus far have focused on the detection of relatively uniform shapes, lines, and patterns, differing from the more irregular and complex shapes found in natural, vegetated environments.

Puissant et al. first introduced the use of texture analysis in kernels to improve the accuracy of land use/land cover classifications on high resolution satellite imagery, showing that texture measures of homogeneity in pixel groups increased accuracy compared to per-pixel texture measures (Puissant et al., 2005). Graesser et al. first proposed utilizing multiple kernel sizes, arguing that multiple measures were necessary to capture and identify urban settlements based on their spatial characteristics at different scales (Graesser et al., 2012). One very common texture analysis, the gray-level co-occurrence matrix (GLCM), analyzes the spatial relationship of gray tones over the pixel window. However, several studies identified additional texture measures that are useful for identifying urban settlements as well (Bayram et al., 2011; Ella et al., 2008; Y. Zhang et al., 2020). Bayram et al. demonstrated that texture measures were also useful to distinguishing cover types, and certain texture measures perform better for some cover types over others (Bayram et al., 2011). Zhang et al. demonstrated that the use of one texture measure alone for classification resulted in poor accuracy while the combination of multiple texture measures (up to about four) increased accuracy (Zhang et al., 2003).

Contextual features have also been used in combination with other datasets such as nighttime lights in order to map urban areas and estimate demographics (Chao et al., 2021; Engstrom et al., 2017, 2019; Sandborn & Engstrom, 2016). Engstrom et al. utilized contextual features to estimate poverty in Sri Lanka and found that spatial features derived from satellite imagery have strong explanatory power for levels of poverty. Similarly, Sandborn & Engstrom (2016) found that spatial features can be used to help map socioeconomic characteristics such as quality of life. Engstrom et al. (2019) also found that contextual features were useful for mapping high-density slums and, when combined, are very strong indicators of urban variability. Despite their successes in these contexts, contextual features remain underutilized for land cover classification purposes, partially because there is still much more to learn about the many ways the combinations of features can be used to effectively characterize and classify other kinds of landscapes.

As demonstrated, Corona imagery presents a unique opportunity to expand our understanding of historic landscape characteristics and fill a knowledge gap regarding grassland conditions prior to periods of intensified degradation and, later, restoration. While previous studies have utilized Corona imagery to derive classified data, these studies have largely engaged in binary classification, or, at most, used only a few clearly discrete classes. The utility of Corona imagery for classifications has not been explored in semi-arid landscapes where distinctions between some classes are less discrete. Similarly, previous studies that have utilized contextual features to derive classified datasets have largely analyzed urban areas and make use of spectral information, which is not available for Corona imagery. Here, we generate a pre-1980s land cover classification of semi-arid

grassland systems in northern China from Corona imagery using spatially derived contextual features, representing a combination of several novel methods and approaches.

4.2 Objectives

The overarching objective was to characterize land cover in Naiman Banner, Inner Mongolia prior to the massive privatization and land use intensification that occurred in the 1980s and 1990s. This provided an opportunity to evaluate the utility of derived surface texture statistics as inputs to a classification algorithm using Corona imagery.

4.3 Study Area

The focal area for this study is the central portion of Naiman Banner, located in the eastern portion of Inner Mongolia about 700 kilometers northeast of Beijing in the Horqin Sandy Lands. A detailed history of the study area, it's location and current conditions is available in chapter two of this thesis.

4.4 Data Collection

4.4.1 Corona Imagery

Corona images were obtained from the USGS's Earth Explorer. Four images, captured on November 30, 1970, were co-referenced to Landsat TM and modern imagery using 80 ground control points. The referencing accuracy of this mosaic is less than 15 meters, which aligns with accuracy values achieved throughout the literature for georeferencing Corona imagery (Casana & Cothren, 2013; Gurjar & Tare, 2019; Nita et al., 2018; Shahtahmassebi et al., 2017). The mosaic has a spatial resolution of 2.5 meters. This process is detailed extensively in chapter three of this thesis. The mosaic was buffered by 600 meters using a buffered clipping geometry of the study area extent which

was applied as the mosaic dataset's boundary mask. The purpose of this was to create a buffer imagery beyond the largest kernel size in the study so that pixels along the study area's boundaries were calculated accurately. In this case, the largest kernel was 500 meters so a buffer of 600 meters was sufficient. The buffered mosaic served as the basis for the contextual features analysis.

4.4.2 Other Imagery

In additional to contextual features, it was hypothesized that the spectral information available for nearest-date Landsat multi-spectral scanner (MSS) imagery would provide additional useful information on variation in surface conditions to the classifier; for instance, to enhance the ability to distinguish between built up areas and vegetated regions with similar textural characteristics. This method would only be applicable for study areas where the coverage and health of vegetation did not change significantly between the datasets. To test this hypothesis, a Normalized Difference Vegetation Index (NDVI) output was generated for the study area using Landsat MSS imagery acquired on June 2, 1976. Bands five (red, 0.6 – 0.7 um) and six (near infra-red (NIR), 0.7 to 0.8 um) were used in the following calculation:

$$NDVI = (NIR - Red) / (NIR + Red)$$

The output was resampled from 60-meter spatial resolution to 25 meters to match the resolution of the contextual feature bands. The spatial variation in the NDVI output is shown in Figure 13.

Figure 13

Landsat MSS NDVI Results (1976)

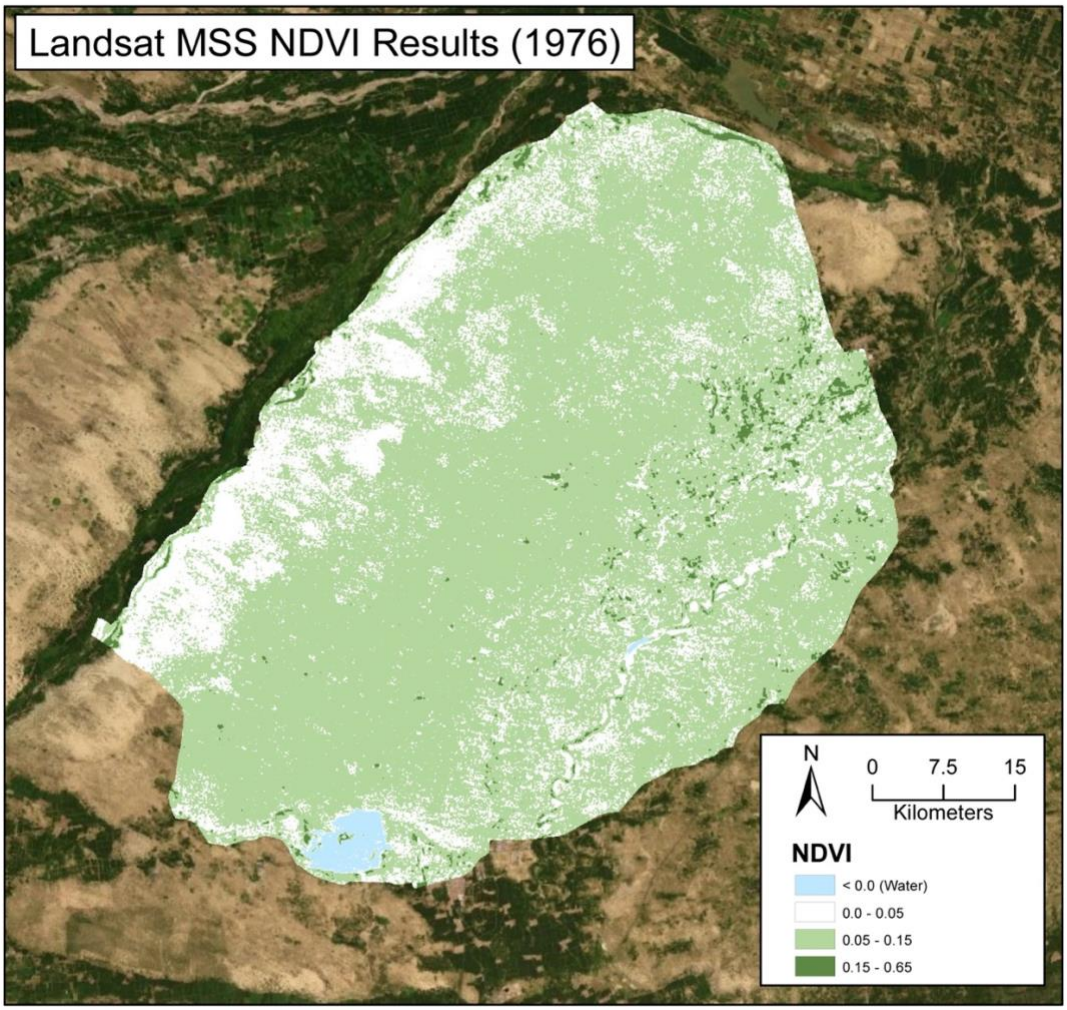

Note. Results of the Landsat MSS NDVI analysis, using bands five (red) and six (near-infrared) of imagery acquired during the growing season in June of 1976

4.5 Methods

4.5.1 Contextual Features Analysis

The contextual features calculated for the mosaic include Fourier (Couteron, 2002; King, 2017; Jensen, 1996), Gabor (Bayram et al., 2011; C. Chen et al., 2015; Yang et al., 2015), Histogram Oriented Gradient (HOG) (Dalal & Triggs, 2005; Graesser et al., 2012; Lei, 2010; Torrione et al., 2014), Lacunarity (LAC) (Graesser et al., 2012; Myint et

al., 2006), Line Support Regions (LSR) (Burns et al., 1986; Unsalan, 2006), Local Binary Pattern (LBPM), Mean (Bolstad, 2019), Oriented FAST and Rotated BRIEF (ORB) (Rublee et al., 2011; J. Xu et al., 2012), PanTex (Pesaresi et al., 2008; Pesaresi & Gerhardinger, 2011), and Structural Feature Sets (SFS) (X. Huang et al., 2007; Sghaier et al., 2017). The utility of each of these features is shown in Table 7. For in-depth descriptions of each feature and additional sources, see Chao et al. (2021).

Multiple window sizes were used in order to assess pixels and their neighborhoods at multiple scales. Each statistic was calculated at scales of 25 meters (10x10 pixel window), 50 meters (20x20 pixel window), 100 meters (40x40 pixel window), and 500 meters (200x200 pixel window) and reported back at a block size of 25 meters, which is the resolution of the outputs (Figure 14) (Engstrom et al., 2019). These window sizes were chosen based on the average size of features in the landscape. Originally, only the scales between 25 and 100 meters were included. Built-up areas were routinely confused with vegetated dunes in early tests due to their textural similarities at finer scales. Since the average built-up area in Naiman Banner in 1970 was smaller than 500 meters in either dimension, it was determined that a slightly larger window size of 500 meters was needed to capture the stark difference in spatial patterning within the settlements and the largely homogenous agricultural fields and pastures that surrounded them. Additionally, vegetated dunes covered contiguous areas of much greater than 500m. While there are undoubtedly elements on the landscape of different sizes than those included here, the scales we chose do cover the most common features. A detailed workflow which is outlined in this section can be seen in Figure 15.

Figure 14

Example of Pixel Window and Block Size

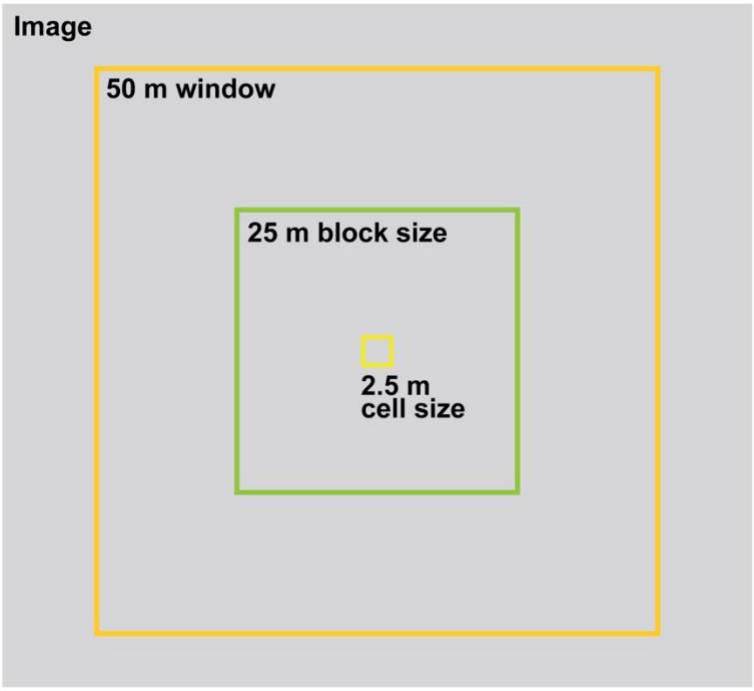

Note. A 2.5-meter cell size with respect to its neighborhood at a scale of 50 meters and the block size of the contextual feature analysis, 25 meters (Adapted from Chao et al., 2021)

Table 7

Contextual Feature Descriptions

Contextual Feature	**Description**
Fourier	Captures frequency of patterns using amplitudes and frequencies (Couteron, 2002; King, 2017; Jensen, 1996)
Gabor	Detects edges using many linear filters (Bayram et al., 2011; C. Chen et al., 2015; Yang et al., 2015)
Histogram Oriented Gradient (HOG)	Identifies the orientation and magnitude of shades (Dalal & Triggs, 2005; Graesser et al., 2012; Lei, 2010; Torrione et al., 2014)
Lacunarity (LAC)	Measures homogeneity by assessing the spatial distribution of gap sizes (Graesser et al., 2012; Myint et al., 2006)
Line Support Regions (LSR)	Extracts straight lines from imagery (Burns et al., 1986; Unsalan, 2006)
Local Binary Pattern (LBPM)	Assesses homogeneity and detects bright/dark spots, flat areas, and edges (Guoying Zhao et al., 2012; X. Huang et al., 2007; W. Li et al., 2015; Ojala et al., 2002)
Mean	Calculates mean and variance of pixel windows using inverse distance weighting (Bolstad, 2019)
Oriented FAST and Rotated BRIEF (ORB)	Extracts features using corner detection (Rublee et al., 2011; J. Xu et al., 2012)
PanTex	Calculates textural contrast (Pesaresi et al., 2008; Pesaresi & Gerhardinger, 2011)
Structural Feature Sets (SFS)	Assesses homogeneity using direction-lines (X. Huang et al., 2007; Sghaier et al., 2017)

Figure 15

Workflow for Contextual Feature Analysis

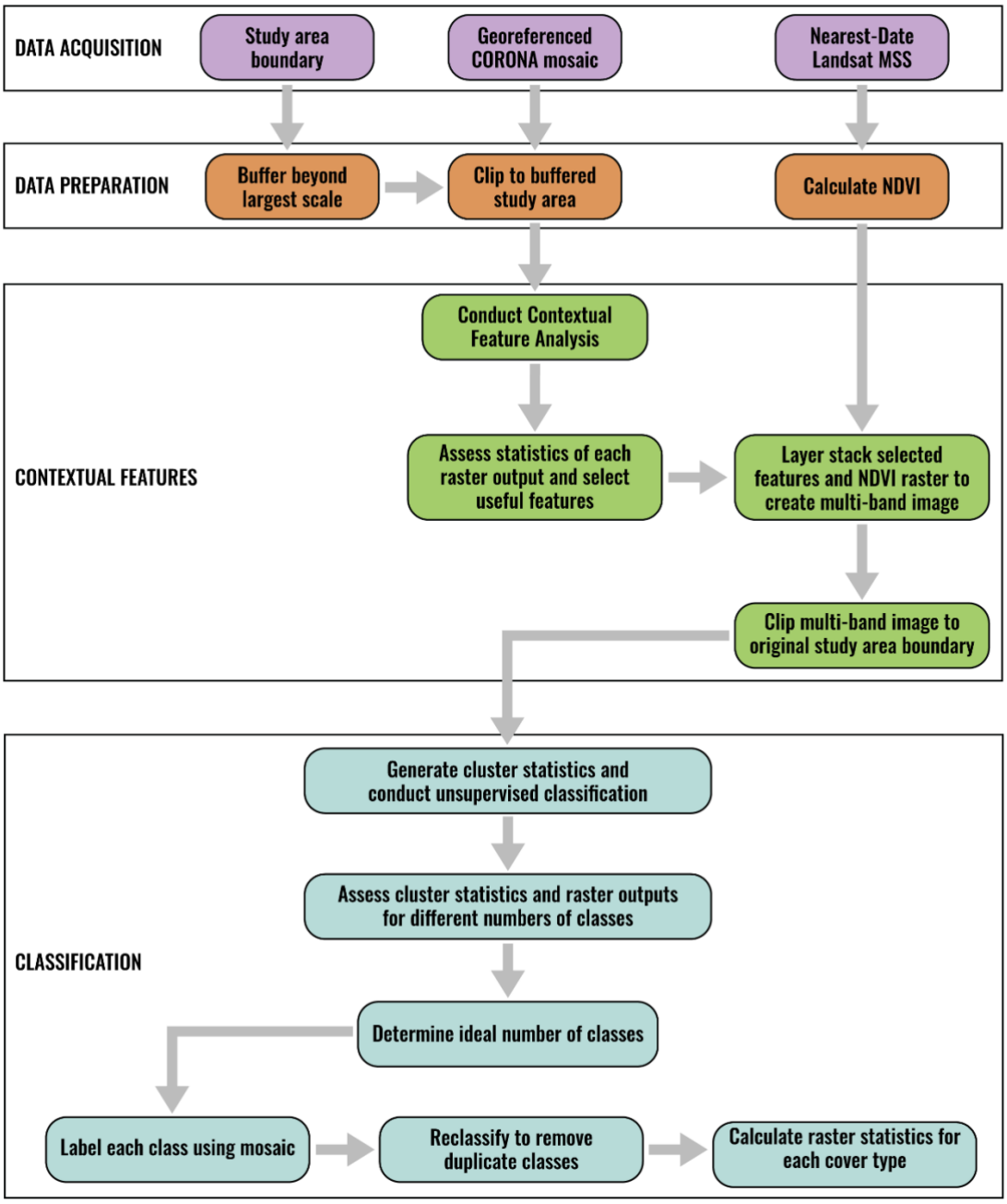

SpFeas (https://github.com/jgrss/spfeas), an open-source Python package developed by Graesser (n.d.) was used to conduct the contextual feature analysis. Due to the computational power required to run contextual features on Corona imagery, scripts

were executed using the George Washington University's supercomputer Pegasus (https://colonialone.gwu.edu/pegasus/). All of the contextual features described in Table 7 were calculated on the buffered Corona mosaic and then clipped to the original bounds of the study area. In total, there were 180 raster outputs which included the contextual feature outputs for each feature at each kernel size. For example, there were eight raster outputs for the Fourier analysis which has two statistical outputs, mean and variance, at four scales (25, 50, 100, and 500 meters. A full list of outputs can be found in Table 8.

Table 8

Contextual Feature Outputs

Feature	**Outputs (at each scale)**	**Total Outputs**
Fourier	Mean and variance	8
Gabor	Mean, variance, orientations 1 through 14	64
HOG	Mean, variance, max, skew, kurtosis	20
LAC	Lacunarity value	4
LSR	Line mean, line length, line contrast	12
LBPM	Mean, variance, max, skew, kurtosis	20
Mean	Mean and variance	8
ORB	Mean, variance, max, skew, kurtosis	20
PanTex	PanTex value	4
SFS	Mean, mean (w), standard deviation, max line length, max angle	20
TOTAL OUTPUTS		180

4.5.2 Determining Appropriate Contextual Features and Creating Multi-Band Images

Because little is known about the use of different combinations of contextual features in applications such as this, an iterative approach for determining useful features was used. Each contextual feature output was assessed visually for its ability to distinguish between potential cover types. Additionally, the histogram of each output was analyzed in order to better understand its range of pixel values. Normally distributed histograms across a greater range of values were preferred over highly skewed or leptokurtic distributions where pixel values fell into a narrow range because, in theory, a larger spread of values would be more useful for distinguishing between cover types. A conservative list of the most descriptive 27 outputs was generated. These outputs were stacked with the Landsat MSS NDVI output to create a multi-band image containing 28 bands.

Clustering was performed in ERDAS Imagine using the ISODATA algorithm in order to iterate through multiple contextual feature combinations. The first iteration of contextual features contained fourier, gabor, HOG, mean, LSR, LBPM, and ORB features at various scales. For the second iteration, confused or mixed classes were identified, and additional useful bands were added based on their ability to differentiate between those classes. Iteration 2 included the same contextual features but was expanded to include additional metrics and scales. The first two iterations only included the 25-, 50- and 100-meter scale outputs. Based on the results of the first two iterations, and continued confusion between the built-up and vegetated classes, an additional 500-meter scale was added. The 500-meter scale was added because it was expected to account for the larger spatial size of built-up areas relative to other classes. As described

previously, this hypothesis was based on the spatial patterning of built-up areas and vegetated dunes, which were consistently confused in both of the initial iterations.

Iteration 3 combines the first, more conservative iteration with four additional contextual feature outputs derived at the 500-meter scale (fourier mean, LSR line mean, LBPM max, and ORB variance). Iteration 4 combines the second, more expansive iteration with the same four additional outputs. In total, there were four different multi-band images and output classifications to compare (Table 9). Based on a visual inspection of the classified outputs, it was determined that Iteration 3 produced the output with the best separation between classes. This iteration represents the contextual features at all four scales that most clearly separate between cover types.

Table 9

Contextual Features and Scales Used in Each Iteration of Unsupervised Classifications (scales indicated in parenthesis, in meters)

Iteration 1	**Iteration 2**	**Iteration 3**	**Iteration 4**
Fourier—Mean (25, 50, 100) Gabor—Mean (100) HOG—Variance (100); max (25) Mean—Mean (25, 50); variance (50, 100) LSR—Line length (100); line mean (100) LBPM—Variance (50, 100); max (25, 50, 100); skew (100); kurtosis (25, 50) ORB—Mean (100); variance (100), kurtosis (100)	Fourier—Mean (25, 50, 100); variance (25, 50, 100) Gabor—Mean (25, 50, 100); variance (25, 50, 100) HOG—Variance (100); max (25) Mean—Mean (25, 50); variance (50, 100) LSR—Line length (100); line mean (100) LBPM—Variance (25, 50, 100); max (25, 50, 100); skew (25, 50, 100); kurtosis (25, 50) ORB—Mean (25, 50, 100); variance (25, 50, 100), kurtosis (25, 50); max (100)	Fourier—Mean (25, 50, 100, 500) Gabor—Mean (100) HOG—Variance (100); max (25) Mean—Mean (25, 50); variance (50, 100) LSR—Line length (100); line mean (100, 500) LBPM—Variance (50, 100); max (25, 50, 100, 500); skew (100); kurtosis (25, 50) ORB—Mean (100); variance (100, 500), kurtosis (100)	Fourier—Mean (25, 50, 100, 500); variance (25, 50, 100) Gabor—Mean (25, 50, 100); variance (25, 50, 100) HOG—Variance (100); max (25) Mean—Mean (25, 50); variance (50, 100) LSR—Line length (100); line mean (100, 500) LBPM—Variance (25, 50, 100); max (25, 50, 100, 500); skew (25, 50, 100); kurtosis (25, 50) ORB—Mean (25, 50, 100); variance (25, 50, 100, 500), kurtosis (25, 50); max (100)

Accounting for Variations in Brightness in Corona Imagery

Despite using color balancing techniques to account for variations in brightness between Corona images, there were persistent differences in the underlying pixel values between Corona images that could not be reconciled. This was apparent after generating the contextual features and conducting the classifications because features in the uppermost portion of the mosaic (consistent with image #1 in chapter three) clustered

differently than the rest of the mosaic. In order to rectify this, the multi-band image containing the selected contextual features and NDVI output was segmented into two parts and the cluster statistics and classified outputs were performed on each part and then merged back together. While it is recommended to properly balance the brightness variations in the Corona mosaic and standardize pixel values prior to the contextual feature analysis, this served as a standout approach for accomplishing a similar final result.

4.5.3 Unsupervised Classification

Once a final multi-band image was selected (iteration 3) and segmented into two study area parts, a more refined unsupervised classification was conducted within R Studio using the CLARA package so that additional metrics regarding cluster separability could be drawn from the classification process. Separability between classes was iteratively assessed with different numbers of clusters by calculating cluster isolation, silhouette index, and within-cluster dissimilarity (Dudek, 2020; Shirkhorshidi et al., 2015). However, these metrics were unable to identify any meaningful pattern of separability between clusters, likely due to the large amount of variability in the underlying statistics in different contextual feature bands. Interestingly, despite there being little evidence based on these metrics that classes were more or less separable with a different number of clusters, the outputs of classifications with different cluster sizes did in fact change the composition of different classes in an impactful way. It was determined through visual inspection that increasing the number of clusters improved the accuracy of the classification consistently until around 60 classes. Then, the results plateaued, and new clusters no longer meaningly broke down into unique clusters that

could represent different cover types. In summary, rather than utilizing cluster separability metrics to determine the ideal number of final classes, this process relied on executing the classifier at many different cluster sizes and visually assessing each output. Ultimately, 60 clusters produced the highest quality output of segmented cover types for both parts of the study area. With each of the final 60-class images, classes were visually assessed and reclassified to eight unique classes. Finally, the two classified images were merged together to create one final land cover dataset.

4.6 Results

The final classified output contains eight unique classes. Based on visual inspection and expert knowledge on the ground we identified the following thematic classes: Built-up area, cropland, pasture, wetland, woody shrub, fixed dune, semi-fixed dune, and mobile dune. The total area of these classes is shown in Table 10, with the three classes of dunes composing the largest percent of the landscape (66.59% combined; 25.54% fixed dunes, 26.73% semi-fixed dunes, and 14.32% mobile dunes). Pasture accounted for 24.76%. The remaining four classes accounted for less than ten percent of the landscape combined. Woody shrub accounted for 2.73%, cropland accounted for 2.55%, built-up area accounted for 1.78%, and wetlands accounted for 1.59%. The final classified image of cover types for the entire study area is shown in Figure 16. Figure 17 shows examples of each cover type in the reference Corona imagery.

These land cover classes represent a more granular depiction of a semi-arid landscape than is typically available for grassland ecosystems from contemporary global land cover datasets. Most studies characterize these landscapes using a few broad cover types, including grassland, barren/sparsely vegetated/unused land, cropland, and built-up

(L. Xu et al., 2018; Xue et al., 2021). These cover types, while useful for describing trends across large scales, are insufficient for describing changes that are occurring within these broad cover types, such as the gradient of vegetation cover that is strongly linked to dune stabilization (Zhou et al., 2015). While it was initially unclear what cover types could be extracted using contextual features given the exploratory nature of this analysis, it became clear when segmenting clusters in the classifier and merging clusters to form cover types that the classifier was able to extract a great amount of detail from the landscape and was able to segment between cover types in far greater detail than is available for other land cover datasets from this time. Because this information was successfully extracted using contextual features, it was worthwhile to maintain them in the final land cover dataset rather than reducing them to broad cover types in order to preserve this important information for better understanding and monitoring grassland degradation.

Table 10

Area of Final Land Cover Classes

Class Name	Area (sq. km)	Area (%)
Semi-fixed Dune	621.18	26.73%
Fixed Dune	593.67	25.54%
Pasture	575.41	24.76%
Mobile Dune	332.87	14.32%
Woody Shrub	63.40	2.73%
Cropland	59.38	2.55%
Built-Up	41.41	1.78%
Wetlands	36.84	1.59%

Figure 16

Land Cover Dataset for Naiman Banner (1970)

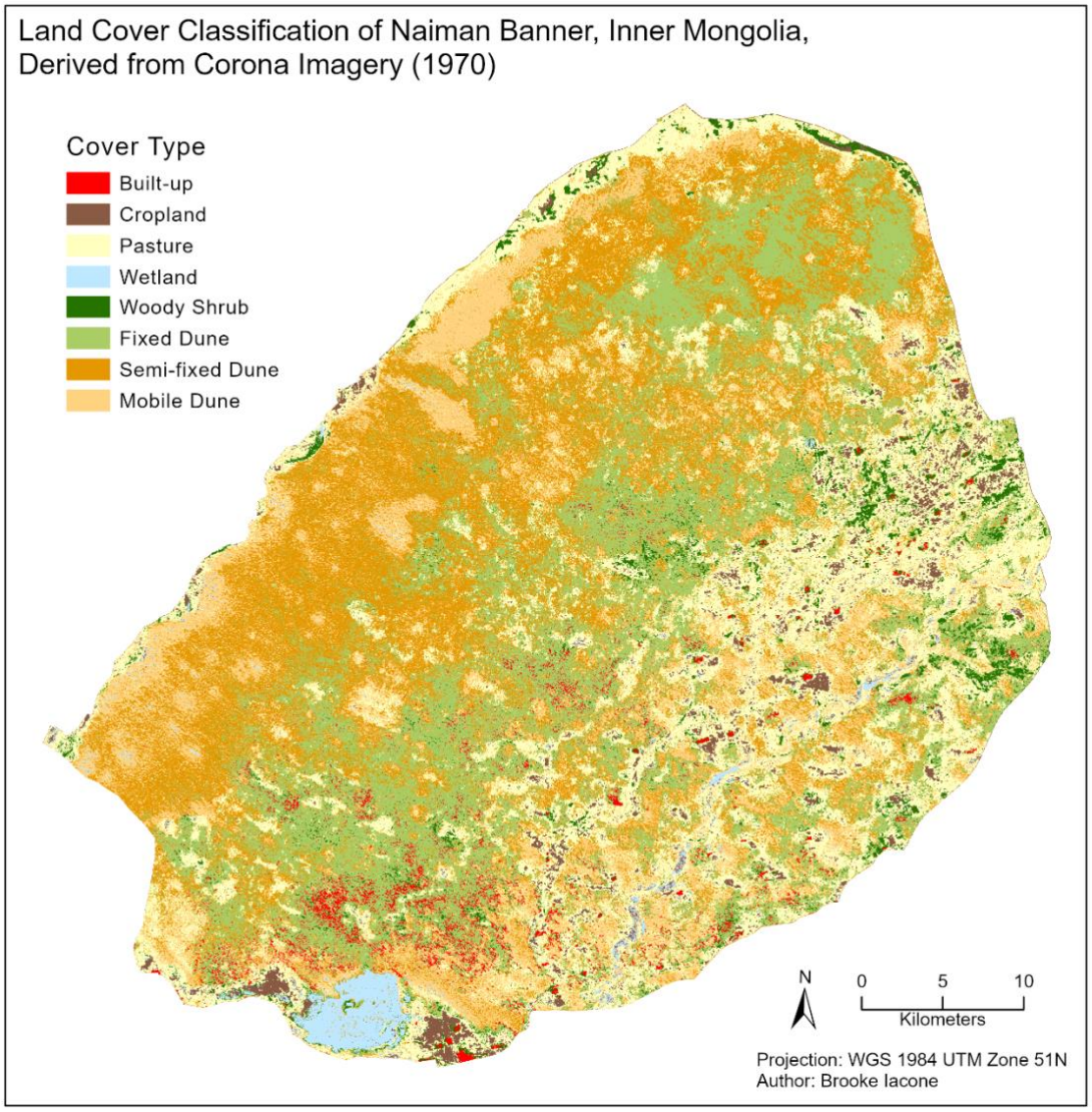

Note. Results of the unsupervised classification identifying land cover types in Naiman Banner, Inner Mongolia using contextual features derived from Corona imagery

Figure 17

Land Cover Classes

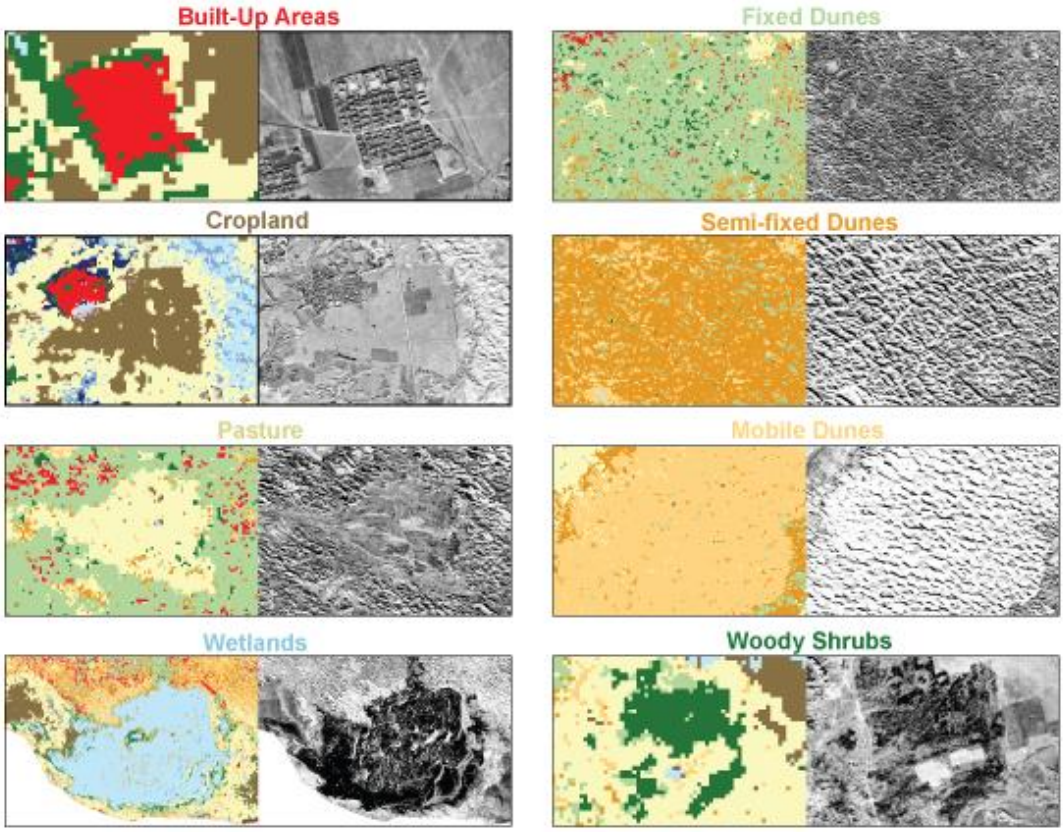

Note. Example of each cover type compared to the reference Corona imagery

4.6.1 Description of Land Cover Types and Assessment of Class Accuracy

Built-Up Area

Built-up area consists of small settlements throughout the landscape, typically composed of grid-like rows of buildings. As mentioned throughout the methodology, built-up area was consistently confused with fixed dunes, likely due the similarity between pixel values and other contextual similarities like line length and orientation. While the iterative process of selecting contextual features and including an additional scale of 500 meters did significantly reduce the mixing of these classes, there is still a moderate amount of fixed dune area that was classified as built-up area, particularly in

the dunes above the present-day city of Naiman. This led to an overestimation of built-up area. However, other built-up areas throughout the landscape are accurately classified with the exception of two settlements which were classified as woody shrub. Since there were a small number of settlements in 1970 and they were fairly easy to pick out manually, an adjusted built-up area estimate was calculated by segmenting out the pixels within actual settlements. A more accurate prediction of built-up area in the study area is 4.4 square kilometers, or 0.18% of the total landscape. The total area of overestimated built-up area was roughly 37 square kilometers.

Cropland

Cropland represents primarily agricultural fields. These features are typically flat, rectangular and homogenous and are located primarily surrounding settlements and clustered around water sources and road networks. This class accurately identified much of the cropland in the landscape. However, this cover type may be underestimated due to mixing with the pasture class. This is likely due to them frequently being located in close proximity, consistent with the land uses surrounding small settlements, and their homogenous characteristics. Fields with brighter/higher pixel values, likely unplanted and/or dry cropland, was most likely to mix with pasture. Darker/lower pixel value cropland, which is likely planted and moister, was sometimes misclassified as wetland.

Pasture

Pasture, also referred to as grassland, rangeland, meadow, or prairie, is a diverse cover type that generally consists of flat, open, vegetated areas that typically serve as grazing land for livestock. This cover type consists of grasses and a mix of annual and perennial forb species. Pasture can be found surrounding small settlements and cropland

as well as in isolation within dune patches. The shape and texture of pasture areas in the landscape varied, from flat and homogenous to complex patch shapes with dotted vegetation. Despite the several types of contrasting spatial patterning, the classifier accurately identified much of the historic pasture area. This class may be slightly overestimated due to the inclusion of some cropland and some noise occurring in the mobile and semi-fixed dunes.

Wetland

Wetland consists of flooded or partially flooded sandy areas and floodplains. This class contains the only surface water sources found throughout the study area. It is composed almost entirely of the distinct wetland area to the west of the city of Naiman. Around 1970 when Corona imagery was acquired, this area consisted of many oases and sandy banks. Sometime in the early 1980s, this area was dammed and flooded for irrigation and as of present day, has been converted to cropland. The sandy floodplains of a river on the eastern portion of Naiman is also captured in this class, which have also been converted to cropland in more recent years. There is a very small amount of mixing with the mobile dune class, which is most likely due to the fact that both consist of exposed sandy areas consisting of bright pixel values, and the cropland class where fields were very dark due to moisture.

Woody Shrub

This class consists of densely aggregated patches of vegetation that are often dark in color, scattered throughout the landscape, most likely woody shrubs and small trees. Overall, this class is only partially representative of this cover type. While the classifier did correctly separate these dark patches of vegetation, it also incorrectly identified some

small built-up areas as woody shrub and introduced some noise into the built-up class. Additionally, some fixed dunes with denser vegetation cover were also classified as woody shrub, likely because there are shrubs on the more stabilized dune surfaces Similar to the findings with built-up areas, the classifier was unable to distinguish between cover types with similar pixel values and spatial patterning, which was the case for built-up areas, fixed dunes, and dense shrub cover. However, this class was still segmented from fixed dune and built-up area in order to capture those unique woody shrub patches.

Fixed Dune

Fixed dune contains dunes that are stabilized by a continuous surface of herbaceous vegetation which prevents movement due to wind and erosion (Figure 18). This class is differentiable in the Corona imagery from both semi-fixed and mobile dunes because of its darker pixel values due to the presence of consistent grass cover and some larger vegetation species. The vegetation cover found in areas with more stable dunes is also seen in the Landsat MSS NDVI result (Figure 13) and corresponds to the fixed dune class. Fixed dunes also contain very little exposed sand and therefore do not possess the typical linear and curved lines formed by more dynamic dune types.

For these reasons, the classifier was able to differentiate between the various dune types quite well. However, it should be noted that dunes are not discrete cover types and often exist along a gradient, shifting between states of fixture and movement depending on the presence and health of the vegetation. Therefore, differences between dune classes can be ambiguous and largely up to the interpretation of the inspector. However, since one of the main objectives of this study is to characterize the conditions of grasslands prior to intensified cultivation and grazing pressure, it was useful to segment the dune

classes as granularly as possible. This allows us to assess the extent and coverage of healthy vegetation across a gradient rather than in one discrete class.

Figure 18

Example of Fixed Dune Dominated by Grasses

Semi-Fixed Dune

This class consists of dunes that have more exposed soils that are only partially stabilized by vegetation and are therefore more susceptible than fixed dunes to movement and erosion (Figure 19). Semi-fixed dunes represent the transition between fixed and mobile dunes, often occurring during the process where fixed dunes become degraded due to loss of vegetation and subsequent soil erosion, eventually leading to desertification. This class differs spatially from fixed dunes and mobile dunes because it contains less vegetated cover (dark pixels) than fixed dunes and less exposed sand (bright pixels) than mobile dunes. This class captures the gradient between both, generally consisting of a lot of short, irregular textures. It is often found co-occurring in speckled and striped patterning with mobile dunes due to the presence of the bright sand. This

heterogenous pattern is often associated with desertification because of decreased density in grass coverage (Liu et al., 2019).

Figure 19

Example of Semi-Fixed Dune

The landscape contains patchy coverage of stabilizing vegetation and mobile sand, captured recently in Naiman Banner (Allington, 2009)

Mobile Dune

The mobile dune class consists of dunes that contain little to no vegetation and have unstable surfaces that shift due to erosion and wind exposure (Figure 20). These dunes are characterized by linear patterns and shadows that form when sand accumulates due to wind. This class typically contains very bright pixel values from exposed sandy surfaces along with the short, dark lines characteristic of the dune shadows. Given their unique spatial patterning, mobile dunes were classified very distinctly, particularly for the large dune fields along the western edge of the landscape. As mentioned previously, this

class typically mixed with semi-fixed dunes and contains some noise from other classes, usually as individual pixels.

Figure 20

Example of Mobile Dunes

4.6.2 Landsat MSS NDVI Evaluation

The classifier was tested with and without the inclusion of the Landsat MSS NDVI in order to assess the approximately contribution of the vegetation index for segmenting between cover types. The classifier performed better with the inclusion of the spectral information. The results were negligible for most cover types, but the vegetation index was particularly useful for detecting and segmenting the woody shrub cover type. The woody shrubs displayed very similar spatial patterning at similar scales as built-up areas, and while there is still come class confusion between woody shrubs and built-up areas, without the inclusion of the vegetation index, the classifier consistently segmented these two cover types together. Given that woody shrub encroachment is an indicator of desertification, this is an important cover type to identify for further analysis and

comparisons over time. Additional information about the contribution of the Landsat MSS NDVI input, perhaps using variable importance indicators, may be useful to quantify it's exact contribution in the classification (Chen et al., 2020).

4.6.3 Accuracy Assessment

In order to evaluate the overall accuracy of the unsupervised classification, an accuracy assessment which compared the cover types identified in the classification against ground truth data was conducted. The purpose of the accuracy assessment was to evaluate how well the classification performed in terms of noise and confusion between classes rather than how accurately it actually identified cover types on the ground, since there are no historic land cover datasets to definitely determine the cover types in the year of the Corona imagery. Because of this lack of available information to compare against, ground truth data in this accuracy assessment refers to a manual inspection of the Corona mosaic from which the land cover classification is derived. While this is not a traditional approach for conducting an accuracy assessment because the ground truth data is derived from the same source as the classification, it was still a useful exercise for comparing the general fidelity of the classification to expert interpretation of cover and therefore, the success of utilizing contextual features to generate cover types.

The classification was evaluated using overall accuracy, kappa coefficient, and class-specific user and producer's accuracies in a confusion matrix. A stratified random sampling method was used to generate 406 points across the eight classes, with the number of points per class proportional to the class area. Classes with smaller areas, such as built-up areas, woody shrubs, and wetlands, contained as few as ten points while the largest cover type by area, semi-fixed dunes, contained 107 points.

The results of the accuracy assessment can be found in Table 11. The overall accuracy was 70.68% and the kappa coefficient was 0.62. In general, the dune classes performed best while built-up area and woody shrub performed poorest. This was to be expected for built-up areas considering the large amount of mixing with the dune classes and given the small sample size. The pasture class performed poorly in terms of having overlap with nearly every other class.

Dune classes were most likely to be misclassified as other dune classes rather than any other cover type. This is significant because, while misclassified, dunes were still identified as dunes. Additionally, some mixing of these classes is to be expected due to the gradient between these cover types. This is important when considering the overall accuracy of this classification, because this analysis ultimately segment classes in above-average granularity in order to better describe characteristics of land degradation occurring in the landscape, including the detection of stabilizing perennial vegetation cover by segmenting dune types by their level of stability. If broad cover types were used for segmenting, such as the typical barren vs. grassland classes used in most large-scale land cover classifications, the overall accuracy would increase significantly. However, as mentioned previously, it was worthwhile to extract a greater level of detail here for maximizing the amount of information extracted from the contextual features and to increase our understanding of the state of grasslands more granularly than simply by capturing them under one broad cover type.

Table 11

Results of Accuracy Assessment of Contextual Feature-Based Unsupervised Classification on Corona Imagery

	Built-Up	Cropland	Pasture	Wetlands	Fixed Dune	Semi-fixed Dune	Mobile Dune	Woody Shrub	Total	User Accuracy	Kappa
Built-Up	1	0	0	0	4	3	2	0	10	**0.1**	0
Cropland	0	7	1	1	0	0	1	0	10	**0.7**	0
Pasture	0	11	65	4	7	3	9	0	99	**0.656**	0
Wetlands	0	0	1	8	0	0	1	0	10	**0.8**	0
Fixed Dune	0	1	0	1	79	16	4	1	102	**0.774**	0
Semi-fixed Dune	0	0	8	1	4	81	13	0	107	**0.757**	0
Mobile Dune	1	1	3	1	1	6	44	0	57	**0.771**	0
Woody Shrub	0	0	1	0	7	0	1	2	11	**0.181**	0
Total	2	20	79	16	102	109	75	3	406	**0**	0
Producer's Accuracy	**0.5**	**0.35**	**0.822**	**0.5**	**0.774**	**0.743**	**0.586**	**0.666**	**0**	**0.706**	0
Kappa	0	0	0	0	0	0	0	0	0	**0**	**0.629**

4.7 Discussion

This analysis represents the first land cover dataset of Naiman Banner for this time period, and therefore has greatly increased our knowledge of the historic landscape characteristics prior to the intense grassland degradation that the region, and northern China at large, experienced beginning at the end of the 1970s with the opening of China's economy and privatization of grasslands. Additionally, this analysis demonstrates a novel approach to utilizing Corona imagery and contextual features for deriving historic land cover data. Further, the results illustrate that surface texture analyses are useful for extracting cover types in above-average detail when compared to dominant spectral approaches for semi-arid landscapes.

4.7.1 Characterizing Naiman Banner's Landscape in 1970

Many differences are observed between the historic and contemporary conditions present in Naiman Banner. First, the extent of built-up areas and cropland have expanded significantly while surface water and pasture areas have drastically decreased. Most of the settlements identified in 1970 have doubled or tripled in size and additional built-up areas and industrial sites have been added, particularly in the eastern half of the study area. Cropland has greatly expanded, replacing much of the area identified as pasture and nearly all of the wetland areas from 1970. Most notably, the large wetland area to the west of the city of Naiman has been converted entirely to cropland. There is little to no surface water remaining today in the study area.

Second, the extent of fixed dunes has decreased while semi-fixed and mobile dunes have increased, indicative of grassland degradation and increased desertification. This is particularly significant because this land cover dataset was derived using non-

growing season imagery captured in November of 1970. Even when compared against contemporary imagery from the growing season, the extent of stabilizing vegetation has still significantly decreased. This not only demonstrates a trend towards increasingly barren or sparsely vegetated areas, but that the vegetation present in 1970 is likely a representation of the historically dominant perennial grasses that once covered these dunes and have been proven to provide greater stabilization than annual vegetation and woody shrubs (Zhou et al., 2015). The fixed dunes identified primarily in the central portion of the study area are now sandier and the vegetation coverage is patchier and fragmented with cropland. Areas identified as mobile dunes in 1970 were more constrained in 1970 than their extent today.

4.7.2 Comparison to ESA World Cover Data

The European Space Agency (ESA) maintains a global 10-meter land cover dataset derived from Sentinel-1 and 2 imagery (Zanaga, Daniele et al., 2021). This dataset contains broad cover types and utilizes standardized methods to categorize cover types across large areas. Since there are very few land cover datasets available for Naiman Banner, past or present, it was hypothesized that ESA'a World Cover data could serve as a contemporary source of comparison. However, this comparison is partially unproductive. In addition to the fifty-year gap between the datasets, some cover types identified in the two classifications do not match up in a meaningful or comparable way. ESA's bare/sparse vegetation and grassland classes both encompassed some of the three types of dunes, woody vegetation, and pastures identified in this study, making it difficult to make class to class comparisons. For these reasons, it is impossible to make

quantitative comparisons of land cover change over time between the results of this study and any contemporary large-scale land cover classifications.

4.7.3 Comparison to Historic Topographic Maps

From the 1960s to the 1980s, the United Socialist Soviet Republic (U.S.S.R.) conducted large-scale mapping of portions of eastern Mongolia and Inner Mongolia for military use (Figure 21). These maps are highly detailed and include settlements, road networks, and even differing dune morphology within Naiman Banner. Maps detailing Naiman Banner were released in the year 1970– the same year as the acquisition of the Corona imagery used as the basis of this study. For these reasons, it is a useful exercise to qualitatively compare the results of the Corona-based land cover classification with the topography described in these maps. Additionally, these maps could be digitized in the future in order to validate the results of land cover classifications. This would be helpful for separating the accuracy assessment from the Corona imagery itself.

Figure 21

Mosaic of Scanned Topographic Maps Developed by the U.S.S.R. (1970)

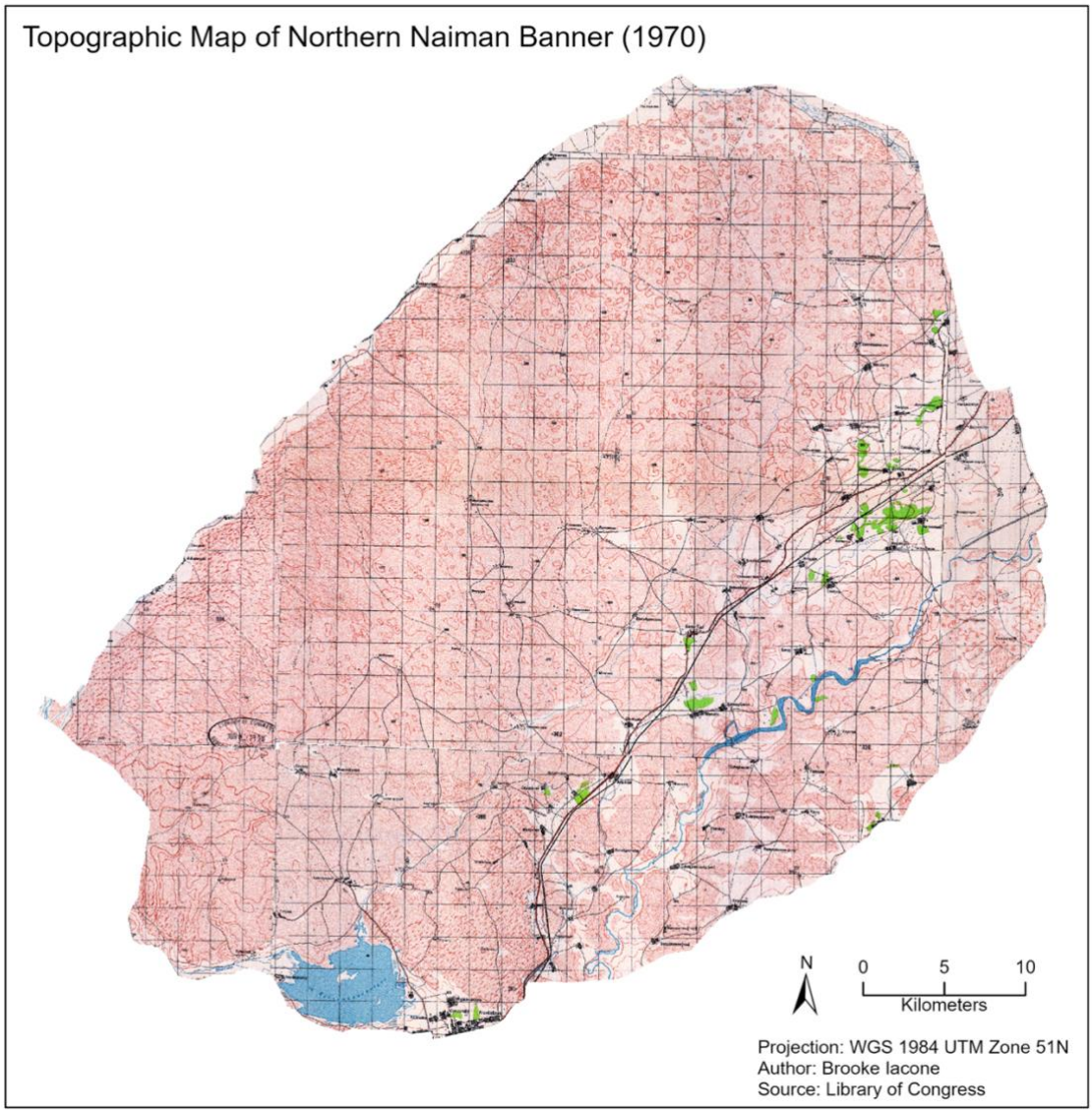

Several notable similarities are present in the topographic maps and the results of the land cover classification. First, the location of wetlands (Figure 22, A) and built-up areas (Figure 22, B) are consistent. Second, flat topography—identified as a pale shade of pink with no additional hatching in the topography map— are consistent with cropland and pastures (Figure 22, C). Mobile dunes are indicated with a pale pink shading and

diagonal red slashes in the topographic map, which is consistent with the mobile dunes identified north of the city of Naiman. Similarly, Figure 23 shows the mobile dune formations in the western half of the study area (Figure 23, D) intermixed with semi-fixed dunes consistent with a different hatch style (Figure 23, E). The topographic map identifies the highly mobile dune formations in near-perfect alignment with the mobile dune class in the Corona-based classification. This comparison further confirms that the classes identified in the land cover classification are accurate depictions of conditions on the ground in 1970.

Figure 22

Comparison Between the Results of the Corona-Based Classification and USSR Topographic Maps, Centered on Naiman City

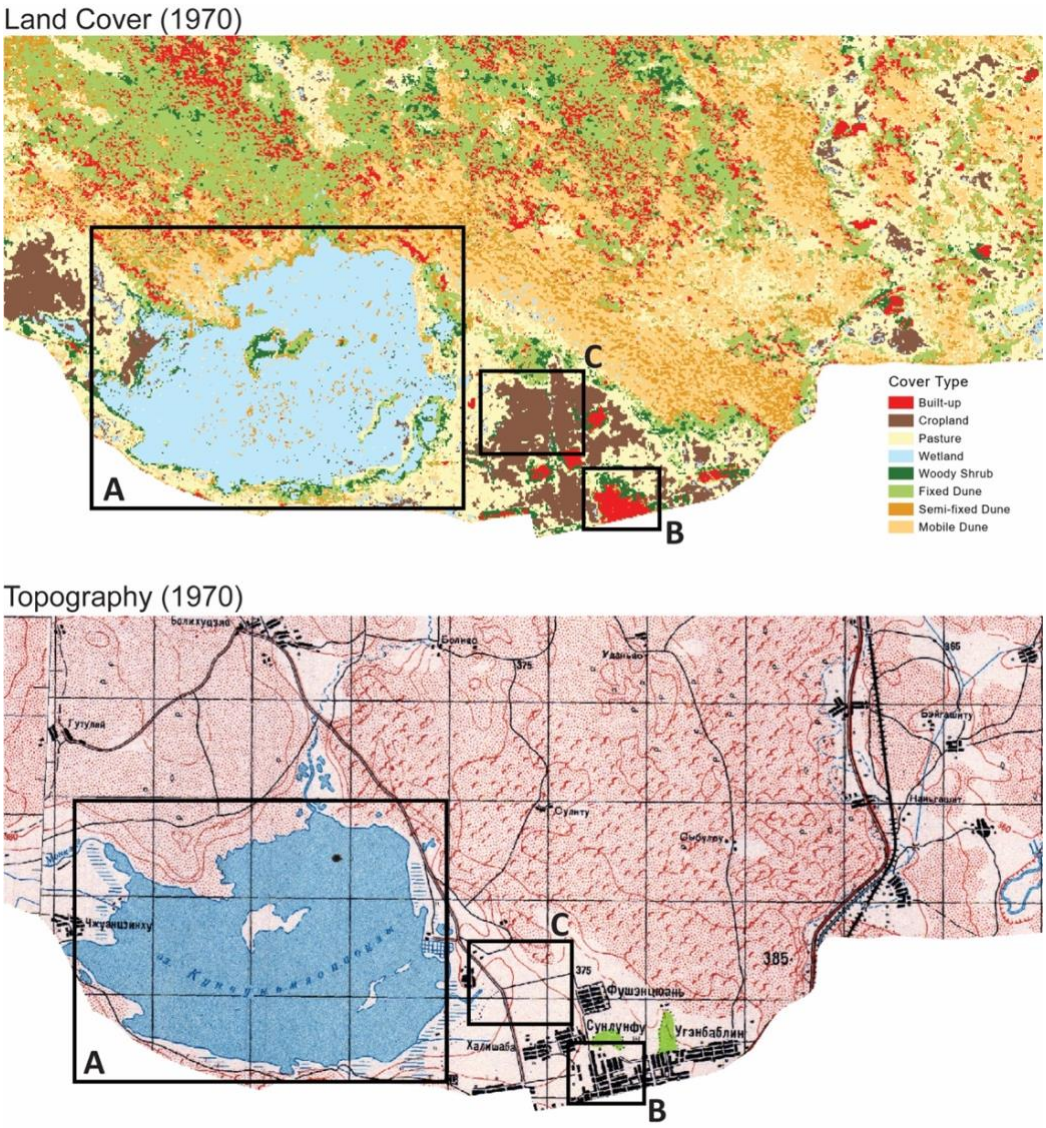

Note. A: Wetlands are consistent, B: Built-up area in present day city of Naiman is consistent, C: Pasture and agriculture classes are consistent with flat topography surrounding Naiman

Figure 23

Comparison Between the Results of the Corona-Based Classification and USSR Topographic Maps, Centered on Western Sand Dunes

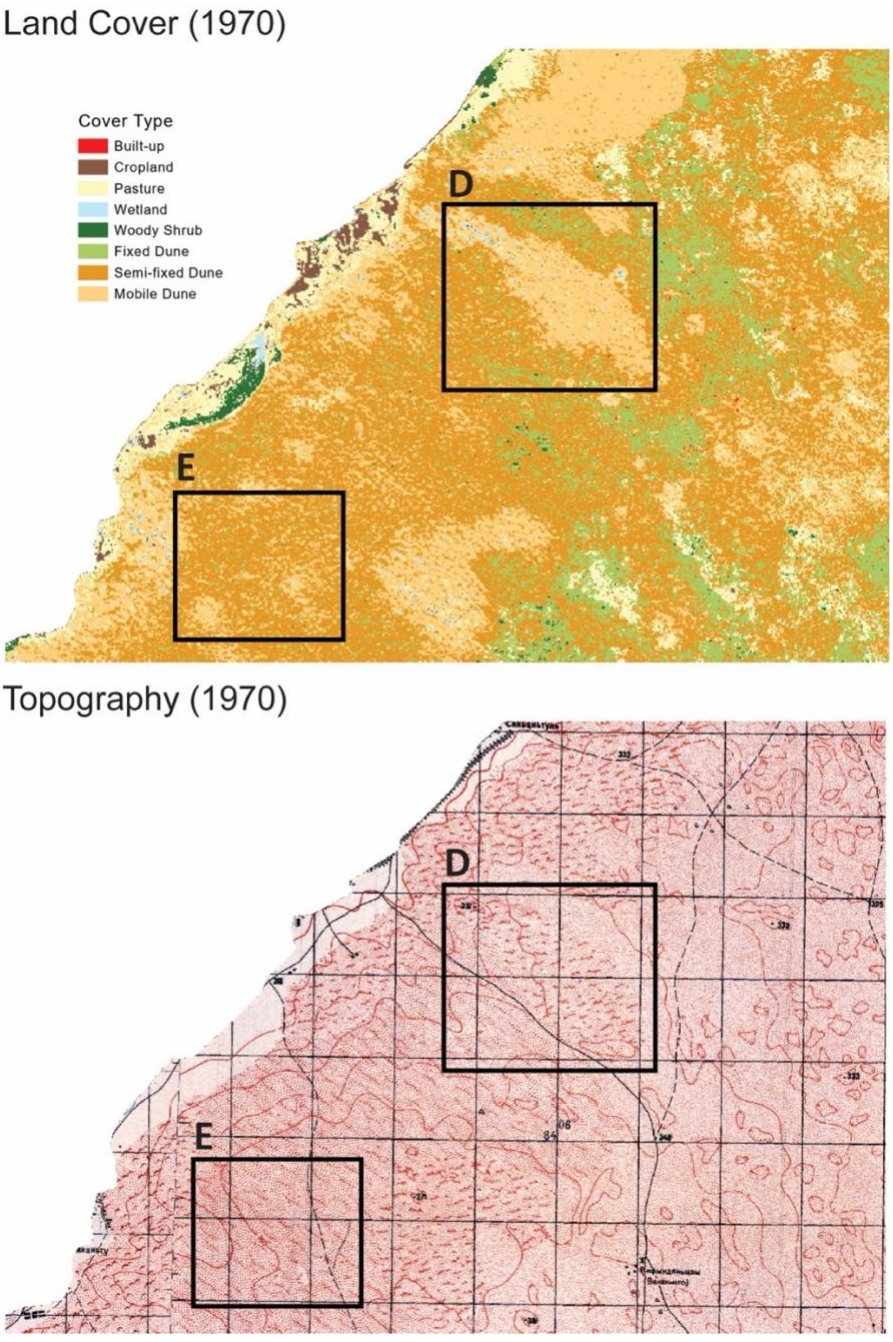

Note. D: Areas identified as mobile dune in the land cover map correspond to a specific type of hatching shown in box D, and the sand dunes are consistent between both datasets. E: Semi-fixed dunes correspond to a different type of hatching that is intermixed with the mobile dunes

4.7.4 Next Steps

These findings suggest that Corona imagery is not only useful for identifying historic cover types but could be useful for making meaningful observations and comparisons between vegetation types present between time periods. Expanding this analysis to include growing-season Corona imagery may inform on what percentage of the landscape is vegetated year-round, and therefore likely stabilized with native perennial grasses. When comparing against contemporary imagery, both in the growing season and non-growing season, this may inform on how the extent of these stabilizing grasses have changed over time through present day, where annual grasses and woody shrubs have overtaken the landscape. This is also informative given that most modern assessments of grassland recovery focus on "greenness". Greenness, while helpful for determining overall vegetation cover, does not describe the type of vegetation present and therefore is not particularly useful in semi-arid landscapes where greenness in the growing season may not be related to long-term recovery of grasslands and stabilization of mobile dunes.

Future studies should utilize the methods and results presented here to assess landscape conditions across multiple time periods in order to further our understanding of long-term grassland degradation and restoration. With the addition of land cover data prior to the 1980s and 1990s, we can now compare these periods of intensified cultivation and grazing pressure, as well as more recent periods of restoration, against the more "baseline" conditions and characteristics detailed here for the 1970s. While previous studies have utilized Corona imagery to compare multiple time periods, these studies only attempted to detect change for one or a few broad cover types (Franklin et al., 2005;

Gurjar & Tare, 2019; Munteanu et al., 2020; Nita et al., 2018; Rendenieks et al., 2020; Rigina, 2003; Saleem et al., 2018; Song et al., 2015; Y. Zhang et al., 2020). In order to make direct comparisons between timepoints at this resolution of detail for cover types, it is necessary to derive the same or comparable cover types on contemporary datasets. Current sources of land cover information, derived mostly using spectral approaches, have had little success achieving this level of detail primarily because spectral analysis of vegetation cover does not perform well in semi-arid environments where the mixing of vegetation and background soil in individual pixels make it difficult to distinguish between cover types. This analysis has demonstrated that contextual features are very useful in semi-arid environments, and that detecting spatial patterns and textures may be more effective than just utilizing spectral profiles to derive cover types. Therefore, there is a great opportunity to extend these methods to contemporary datasets not only to create comparable datasets for change detection analysis and comparison, but to explore the use of new approaches of detecting land cover types in semi-arid environments.

Future work should also expand upon the methods demonstrated here for both their use on Corona and contemporary imagery. This analysis utilized an unsupervised classification approach because this was a novel combination of datasets and methods, and it was largely unknown what cover types could be produced and what the limitations would be, particularly given the complex nature of semi-arid landscapes and unknowns associated with working with Corona imagery. Since contemporary datasets are unable to distinguish between cover types well in semi-arid environments, it was difficult to determine what cover types to collect training data for or what their unique spatial characteristics would be in a decision-tree classifier. Given that this analysis has

demonstrated the ability of contextual features to derive unique and granular cover types, and there are now potential known classes to build upon, future work should refine these methods towards supervised, decision-tree classification approaches, which would likely improve the accuracy of the classification. One such opportunity may be to utilize landscape metrics at the patch and class level as decision-tree nodes for determining a pixel's class. Some cover types were found to be compact (built-up areas, cropland, woody shrub, and wetland) while other cover types existed in patch networks (fixed dunes and pastures) or intermixed with another class in speckled and dispersed patterns (semi-fixed dunes and mobile dunes). Various isolation, patchiness, and network indexes may inform on a pixel's true class based on these characteristics and improve the overall results. For example, built-up pixels within actual settlements with metrics demonstrating compactness would classify as built-up, while the fixed dune areas misclassified as built-up in this analysis would be segmented out based on their speckled and dispersed patterning.

4.8 Conclusion

Despite the limitations of utilizing historic imagery and the present challenges associated with deriving cover types from semi-arid landscapes, this analysis successfully presented a combination of novel approaches utilizing Corona imagery and contextual features to derive the first land cover dataset and assessment of landscape conditions in Naiman Banner for pre-satellite times. Further, this research presents a resolution of detail in dune types and vegetation cover that is not available for this region, past or present, providing a unique opportunity to both assess the conditions of the landscape in far greater detail and expand these methodologies to other points in time. Our

understanding of the landscape will continue to grow as the methods are refined and the analysis is extended to include long-term assessments of change. Understanding historic land cover at this level of detail is necessary for our continued understanding of anthropogenic changes leading to increased desertification and global environmental change.

Chapter 5: Conclusion

This study successfully generated new datasets that will extend the timeline of available data for monitoring grassland degradation and recovery dynamics in northern China. Focusing on the highly degraded region of Naiman Banner, Inner Mongolia, this work generated a historic mosaic from Corona imagery for the year 1970, representing the first qualitative assessment of the landscape for this region at this time. In generating this historic mosaic, a detailed and repeatable methodology for accurately georeferencing Corona mosaic is presented, expanding the limited body of knowledge on the process of utilizing this historic imagery source. This work also generated a historic land cover dataset from the Corona mosaic using derived contextual features and demonstrated that, despite Corona imagery containing no spectral information, these methods were highly effective for extracting land cover information from the landscape. Additionally, this work presents a resolution of detail in dune type and gradients of vegetation cover that was not previously available for this region beyond the broad cover types of grassland and barren land. These complexities are essential for understanding the progression of desertification, state of the soil, and susceptibility to wind erosion. Our understanding of the landscape will continue to grow as the methods presented here are refined and the analysis is extended to include long-term assessments of change.

This thesis expands upon past work that has utilized Corona imagery to extend the timeline of available imagery for analysis by presenting an approach for classifying multiple land cover types. Previous methods have only sought to identify single-focus features such as the presence of absence of forest, but have not characterized an entire landscape, nor have any studies done so in a complex semi-arid grassland system. This

thesis also expands upon past work that has utilized contextual features in combination with spectral information for detecting and characterizing urban areas, demonstrating that contextual features are able to extract a high level of detail for cover types beyond the built environment and with minimum spectral input.

In generating these datasets and exploring a combination of several novel methodologies, this thesis successfully characterizes the landscape of central Naiman Banner prior to the massive privatization and land use intensification that occurred in the 1980s and 1990s. It is clear that the landscape has changed significantly in a number of ways. Built-up areas and cropland have greatly increased, while pasture and fixed dune areas that are characterized by a high percentage of stabilizing vegetation cover have been degraded to patchier semi-fixed areas with simplified vegetation structure. Barren and sparsely vegetated mobile dune areas have increased. Using non-growing season imagery also revealed that there was likely still a significant extent of perennial grasses in the landscape in 1970, all of which has been replaced by annual grasses and woody shrubs. And lastly, any remaining surface water in the landscape has been lost. These findings indicate that Naiman Banner has faced significant grassland degradation, and the landscape has greatly simplified due to the impacts of desertification which have been fueled by on-going damaging anthropogenic activity.

Drylands are vital ecosystems that continue to face the threat of desertification due to degrading land practices. Growing demand for resources from China's grasslands and the impact of periods of intense degradation mean that the long-term health and recovery of northern China's degraded grasslands is still largely unknown despite recent restoration efforts. Their sustained health and recovery is critical not only to protect

biodiversity, but because important ecosystem services are lost when productivity is lost. Long-term or irreversible state changes to the world's drylands threaten food security and increase the impacts of climate change, which has the potential to harm and displace a large portion of the world's population. Therefore, it is critical to analyze long term land use and land cover patterns, and the integration of long-term remotely sensed analysis is essential to our understanding of global environmental change.

References

Allington, G. R. H., Li, W., & Brown, D. G. (2017). Urbanization and environmental policy effects on the future availability of grazing resources on the Mongolian Plateau: Modeling socio-environmental system dynamics. *Environmental Science & Policy*, *68*, 35–46. https://doi.org/10.1016/j.envsci.2016.11.005

Allington, G. R. H., & Valone, T. J. (2010). Reversal of desertification: The role of physical and chemical soil properties. *Journal of Arid Environments*, *74*(8), 973–977. https://doi.org/10.1016/j.jaridenv.2009.12.005

An, Y., Gao, W., & Gao, Z. (2014). Characterizing land condition variability in Northern China from 1982 to 2011. *Environmental Earth Sciences*, *72*(3), 663–676. https://doi.org/10.1007/s12665-013-2987-6

Andersen, G. L. (2006). How to detect desert trees using corona images: Discovering historical ecological data. *Journal of Arid Environments*, *65*(3), 491–511. https://doi.org/10.1016/j.jaridenv.2005.07.010

Archer, S. R., Andersen, E. M., Predick, K. I., Schwinning, S., Steidl, R. J., & Woods, S. R. (2017). Woody Plant Encroachment: Causes and Consequences. In D. D. Briske (Ed.), *Rangeland Systems* (pp. 25–84). Springer International Publishing. https://doi.org/10.1007/978-3-319-46709-2_2

Bayram, U., Can, G., Duzgun, S., & Yalabik, N. (2011). *Evaluation of textural features for multispectral images* (L. Bruzzone, Ed.; p. 81800I). https://doi.org/10.1117/12.898292

Bestelmeyer, B. T., Okin, G. S., Duniway, M. C., Archer, S. R., Sayre, N. F., Williamson, J. C., & Herrick, J. E. (2015). Desertification, land use, and the transformation of

global drylands. *Frontiers in Ecology and the Environment*, *13*(1), 28–36. https://doi.org/10.1890/140162

Bolstad, P. (2019). *GIS fundamentals: A first text on geographic information systems* (6th edition). XanEdu.

Brogaard, S., & Prieler, S. (1998). *Land cover in the Horqin Grasslands, North China. Detecting changes between 1975 and 1990 by means of remote sensing.* 26.

Brovkin, V., Boysen, L., Arora, V. K., Boisier, J. P., Cadule, P., Chini, L., Claussen, M., Friedlingstein, P., Gayler, V., van den Hurk, B. J. J. M., Hurtt, G. C., Jones, C. D., Kato, E., de Noblet-Ducoudré, N., Pacifico, F., Pongratz, J., & Weiss, M. (2013). Effect of Anthropogenic Land-Use and Land-Cover Changes on Climate and Land Carbon Storage in CMIP5 Projections for the Twenty-First Century. *Journal of Climate*, *26*(18), 6859–6881. https://doi.org/10.1175/JCLI-D-12-00623.1

Bryan, B. A., Gao, L., Ye, Y., Sun, X., Connor, J. D., Crossman, N. D., Stafford-Smith, M., Wu, J., He, C., Yu, D., Liu, Z., Li, A., Huang, Q., Ren, H., Deng, X., Zheng, H., Niu, J., Han, G., & Hou, X. (2018). China's response to a national land-system sustainability emergency. *Nature*, *559*(7713), 193–204. https://doi.org/10.1038/s41586-018-0280-2

Burns, J. B., Hanson, A. R., & Riseman, E. M. (1986). Extracting Straight Lines. *IEEE Transactions on Pattern Analysis and Machine Intelligence*, *PAMI-8*(4), 425–455. https://doi.org/10.1109/TPAMI.1986.4767808

Casana, J., & Cothren, J. (2013). The CORONA Atlas Project: Orthorectification of CORONA Satellite Imagery and Regional-Scale Archaeological Exploration in the Near East. In D. C. Comer & M. J. Harrower, *Mapping Archaeological*

Landscapes from Space (Vol. 5, pp. 33–43). Springer New York. https://doi.org/10.1007/978-1-4614-6074-9_4

Chao, S., Engstrom, R., Mann, M., & Bedada, A. (2021). Evaluating the Ability to Use Contextual Features Derived from Multi-Scale Satellite Imagery to Map Spatial Patterns of Urban Attributes and Population Distributions. *Remote Sensing*, *13*(19), 3962. https://doi.org/10.3390/rs13193962

Chen, C., Zhou, L., Guo, J., Li, W., Su, H., & Guo, F. (2015). Gabor-Filtering-Based Completed Local Binary Patterns for Land-Use Scene Classification. *2015 IEEE International Conference on Multimedia Big Data*, 324–329. https://doi.org/10.1109/BigMM.2015.23

Chen, R.-C., Dewi, C., Huang, S.-W., & Caraka, R. E. (2020). Selecting critical features for data classification based on machine learning methods. *Journal of Big Data*, *7*(1), 52. https://doi.org/10.1186/s40537-020-00327-4

Coskun Hepcan, C. (2013). Quantifying landscape pattern and connectivity in a Mediterranean coastal settlement: The case of the Urla district, Turkey. *Environmental Monitoring and Assessment*, *185*(1), 143–155. https://doi.org/10.1007/s10661-012-2539-7

Couteron, P. (2002). Quantifying change in patterned semi-arid vegetation by Fourier analysis of digitized aerial photographs. *International Journal of Remote Sensing*, *23*(17), 3407–3425. https://doi.org/10.1080/01431160110107699

Dalal, N., & Triggs, B. (2005). Histograms of Oriented Gradients for Human Detection. *2005 IEEE Computer Society Conference on Computer Vision and Pattern Recognition (CVPR'05)*, *1*, 886–893. https://doi.org/10.1109/CVPR.2005.177

de Noblet-Ducoudré, N., Boisier, J.-P., Pitman, A., Bonan, G. B., Brovkin, V., Cruz, F., Delire, C., Gayler, V., van den Hurk, B. J. J. M., Lawrence, P. J., van der Molen, M. K., Müller, C., Reick, C. H., Strengers, B. J., & Voldoire, A. (2012). Determining Robust Impacts of Land-Use-Induced Land Cover Changes on Surface Climate over North America and Eurasia: Results from the First Set of LUCID Experiments. *Journal of Climate*, *25*(9), 3261–3281. https://doi.org/10.1175/JCLI-D-11-00338.1

D'Odorico, P., Rosa, L., Bhattachan, A., & Okin, G. S. (2019). Desertification and Land Degradation. In P. D'Odorico, A. Porporato, & C. Wilkinson Runyan (Eds.), *Dryland Ecohydrology* (pp. 573–602). Springer International Publishing. https://doi.org/10.1007/978-3-030-23269-6_21

Dong, J., Tao, F., & Zhang, G. (2011). Trends and variation in vegetation greenness related to geographic controls in middle and eastern Inner Mongolia, China. *Environmental Earth Sciences*, *62*(2), 245–256. https://doi.org/10.1007/s12665-010-0518-2

Dudek, A. (2020). Silhouette Index as Clustering Evaluation Tool. In K. Jajuga, J. Batóg, & M. Walesiak (Eds.), *Classification and Data Analysis* (pp. 19–33). Springer International Publishing. https://doi.org/10.1007/978-3-030-52348-0_2

Ella, L. P. A., van den Bergh, F., van Wyk, B. J., & van Wyk, M. A. (2008). A Comparison of Texture Feature Algorithms for Urban Settlement Classification. *IGARSS 2008 - 2008 IEEE International Geoscience and Remote Sensing Symposium*, III-1308-III–1311. https://doi.org/10.1109/IGARSS.2008.4779599

Engstrom, R., Harrison, R., Mann, M., & Fletcher, A. (2019). Evaluating the Relationship Between Contextual Features Derived from Very High Spatial Resolution Imagery and Urban Attributes: A Case Study in Sri Lanka. *2019 Joint Urban Remote Sensing Event (JURSE)*, 1–4. https://doi.org/10.1109/JURSE.2019.8809041

Engstrom, R., Hersh, J., & Newhouse, D. (2017). *Poverty from Space: Using High-Resolution Satellite Imagery for Estimating Economic Well-Being*. 36.

Feng, Q., Ma, H., Jiang, X., Wang, X., & Cao, S. (2015). What Has Caused Desertification in China? *Scientific Reports*, *5*(1), 15998. https://doi.org/10.1038/srep15998

Fourier Transform. (2017). In M. King, *Statistics for Process Control Engineers* (pp. 305–313). John Wiley & Sons, Ltd. https://doi.org/10.1002/9781119383536.ch19

Franklin, S. E., Montgomery, P. K., & Stenhouse, G. B. (2005). Interpretation of land cover changes using aerial photography and satellite imagery in the Foothills Model Forest of Alberta. *Canadian Journal of Remote Sensing*, *31*(4), 10.

Gao, L., Huang, J., & Rozelle, S. (2012). Rental markets for cultivated land and agricultural investments in China: L. Gao et al./Agricultural Economics 43 (2012) 389-401. *Agricultural Economics*, *43*(4), 391–403. https://doi.org/10.1111/j.1574-0862.2012.00591.x

Graesser, J., Cheriyadat, A., Vatsavai, R. R., Chandola, V., Long, J., & Bright, E. (2012). Image Based Characterization of Formal and Informal Neighborhoods in an Urban Landscape. *IEEE Journal of Selected Topics in Applied Earth*

Observations and Remote Sensing, *5*(4), 1164–1176. https://doi.org/10.1109/JSTARS.2012.2190383

Grasslands and Grassland Sciences in Northern China (p. 1942). (1992). National Academies Press. https://doi.org/10.17226/1942

Grousset, R. (1970). *The empire of the steppes: A history of central Asia*. Rutgers University Press.

Guo, B., & Wen, Y. (2020). An Optimal Monitoring Model of Desertification in Naiman Banner Based on Feature Space Utilizing Landsat8 Oli Image. *IEEE Access*, *8*, 4761–4768. https://doi.org/10.1109/ACCESS.2019.2962909

Guoying Zhao, Ahonen, T., Matas, J., & Pietikainen, M. (2012). Rotation-Invariant Image and Video Description With Local Binary Pattern Features. *IEEE Transactions on Image Processing*, *21*(4), 1465–1477. https://doi.org/10.1109/TIP.2011.2175739

Gurjar, S. K., & Tare, V. (2019). Estimating long-term LULC changes in an agriculture-dominated basin using CORONA (1970) and LISS IV (2013–14) satellite images: A case study of Ramganga River, India. *Environmental Monitoring and Assessment*, *191*(4), 217. https://doi.org/10.1007/s10661-019-7356-9

Hamandawana, H., Eckardt, F., & Ringrose, S. (2007). Proposed methodology for georeferencing and mosaicking Corona photographs. *International Journal of Remote Sensing*, *28*(1), 5–22. https://doi.org/10.1080/01431160500104400

Ho, P. (2000). The Clash over State and Collective Property: The Making of the Rangeland Law. *The China Quarterly*, *161*, 240–263. JSTOR.

Hua, L., & Squires, V. R. (2015). Managing China's pastoral lands: Current problems and future prospects. *Land Use Policy*, *43*, 129–137. https://doi.org/10.1016/j.landusepol.2014.11.004

Huang, J., Wang, X., Zhi, H., Huang, Z., & Rozelle, S. (2011). Subsidies and distortions in China's agriculture: Evidence from producer-level data*: Subsidies and distortions in China's agriculture. *Australian Journal of Agricultural and Resource Economics*, *55*(1), 53–71. https://doi.org/10.1111/j.1467-8489.2010.00527.x

Huang, X., Zhang, L., & Li, P. (2007). Classification and Extraction of Spatial Features in Urban Areas Using High-Resolution Multispectral Imagery. *IEEE Geoscience and Remote Sensing Letters*, *4*(2), 260–264. https://doi.org/10.1109/LGRS.2006.890540

International Union for Conservation of Nature. (2017, June). *Drylands and land degradation*. https://www.iucn.org/resources/issues-briefs/drylands-and-land-degradation

IPBES. (2018). *The IPBES assessment report on land degradation and restoration.* (L. Montanarella, R. Scholes, & A. Brainich, Eds.). Secretariatof the intergovernmental science-policy platform on biodiversity and eco-system services.

Jensen, J. R. (1996). *Introductory Digital Image Processing: A Remote Sensing Perspective*. Prentice Hall, Inc.

Lei, Z. (2010). Histogram of oriented gradient detector with color-invariant gradients in Gaussian color space. *Optical Engineering*, *49*(10), 109701. https://doi.org/10.1117/1.3503944

Li, A., Wu, J., & Huang, J. (2012). Distinguishing between human-induced and climate-driven vegetation changes: A critical application of RESTREND in inner Mongolia. *Landscape Ecology*, *27*(7), 969–982. https://doi.org/10.1007/s10980-012-9751-2

Li, A., Wu, J., Zhang, X., Xue, J., Liu, Z., Han, X., & Huang, J. (2018). China's new rural "separating three property rights" land reform results in grassland degradation: Evidence from Inner Mongolia. *Land Use Policy*, *71*, 170–182. https://doi.org/10.1016/j.landusepol.2017.11.052

Li, J., Xu, B., Yang, X., Jin, Y., Zhao, L., Zhao, F., Chen, S., Guo, J., Qin, Z., & Ma, H. (2015). Characterizing changes in grassland desertification based on Landsat images of the Ongniud and Naiman Banners, Inner Mongolia. *International Journal of Remote Sensing*, *36*(19–20), 5137–5149. https://doi.org/10.1080/01431161.2015.1029596

Li, J., Xu, B., Yang, X., Qin, Z., Zhao, L., Jin, Y., Zhao, F., & Guo, J. (2017). Historical grassland desertification changes in the Horqin Sandy Land, Northern China (1985–2013). *Scientific Reports*, *7*(1), 3009. https://doi.org/10.1038/s41598-017-03267-x

Li, J., Yang, X., Jin, Y., Yang, Z., Huang, W., Zhao, L., Gao, T., Yu, H., Ma, H., Qin, Z., & Xu, B. (2013). Monitoring and analysis of grassland desertification dynamics

using Landsat images in Ningxia, China. *Remote Sensing of Environment*, *138*, 19–26. https://doi.org/10.1016/j.rse.2013.07.010

Li, W., Chen, C., Su, H., & Du, Q. (2015). Local Binary Patterns and Extreme Learning Machine for Hyperspectral Imagery Classification. *IEEE Transactions on Geoscience and Remote Sensing*, *53*(7), 3681–3693. https://doi.org/10.1109/TGRS.2014.2381602

Liu, M., Dries, L., Heijman, W., Zhu, X., Deng, X., & Huang, J. (2019). Land tenure reform and grassland degradation in Inner Mongolia, China. *China Economic Review*, *55*, 181–198. https://doi.org/10.1016/j.chieco.2019.04.006

Miyasaka, T., Okuro, T., Zhao, X., & Takeuchi, K. (2016). Classification of Land Use on Sand-Dune Topography by Object-Based Analysis, Digital Photogrammetry, and GIS Analysis in the Horqin Sandy Land, China. *Environments*, *3*(4), 17. https://doi.org/10.3390/environments3030017

Munteanu, C., Kamp, J., Nita, M. D., Klein, N., Kraemer, B. M., Müller, D., Koshkina, A., Prishchepov, A. V., & Kuemmerle, T. (2020). Cold War spy satellite images reveal long-term declines of a philopatric keystone species in response to cropland expansion. *Proceedings of the Royal Society B: Biological Sciences*, *287*(1927), 20192897. https://doi.org/10.1098/rspb.2019.2897

Myint, S. W., Mesev, V., & Lam, N. (2006). Urban Textural Analysis from Remote Sensor Data: Lacunarity Measurements Based on the Differential Box Counting Method. *Geographical Analysis*, *38*(4), 371–390. https://doi.org/10.1111/j.1538-4632.2006.00691.x

National Reconnaissance Office. (n.d.). *Corona Fact Sheet*. https://www.nro.gov/History-and-Studies/Center-for-the-Study-of-National-Reconnaissance/The-CORONA-Program/Fact-Sheet/

Nita, M. D., Munteanu, C., Gutman, G., Abrudan, I. V., & Radeloff, V. C. (2018). Widespread forest cutting in the aftermath of World War II captured by broad-scale historical Corona spy satellite photography. *Remote Sensing of Environment, 204*, 322–332. https://doi.org/10.1016/j.rse.2017.10.021

Ojala, T., Pietikainen, M., & Maenpaa, T. (2002). Multiresolution gray-scale and rotation invariant texture classification with local binary patterns. *IEEE Transactions on Pattern Analysis and Machine Intelligence*, *24*(7), 971–987. https://doi.org/10.1109/TPAMI.2002.1017623

Pesaresi, M., & Gerhardinger, A. (2011). Improved Textural Built-Up Presence Index for Automatic Recognition of Human Settlements in Arid Regions With Scattered Vegetation. *IEEE Journal of Selected Topics in Applied Earth Observations and Remote Sensing*, *4*(1), 16–26. https://doi.org/10.1109/JSTARS.2010.2049478

Pesaresi, M., Gerhardinger, A., & Kayitakire, F. (2008). A Robust Built-Up Area Presence Index by Anisotropic Rotation-Invariant Textural Measure. *IEEE Journal of Selected Topics in Applied Earth Observations and Remote Sensing*, *1*(3), 180–192. https://doi.org/10.1109/JSTARS.2008.2002869

Pitman, A. J., de Noblet-Ducoudré, N., Cruz, F. T., Davin, E. L., Bonan, G. B., Brovkin, V., Claussen, M., Delire, C., Ganzeveld, L., Gayler, V., van den Hurk, B. J. J. M., Lawrence, P. J., van der Molen, M. K., Müller, C., Reick, C. H., Seneviratne, S. I., Strengers, B. J., & Voldoire, A. (2009). Uncertainties in climate responses to

past land cover change: First results from the LUCID intercomparison study. *Geophysical Research Letters*, *36*(14), L14814. https://doi.org/10.1029/2009GL039076

Prestele, R., Alexander, P., Rounsevell, M. D. A., Arneth, A., Calvin, K., Doelman, J., Eitelberg, D. A., Engström, K., Fujimori, S., Hasegawa, T., Havlik, P., Humpenöder, F., Jain, A. K., Krisztin, T., Kyle, P., Meiyappan, P., Popp, A., Sands, R. D., Schaldach, R., … Verburg, P. H. (2016). Hotspots of uncertainty in land-use and land-cover change projections: A global-scale model comparison. *Global Change Biology*, *22*(12), 3967–3983. https://doi.org/10.1111/gcb.13337

Puissant, A., Hirsch, J., & Weber, C. (2005). The utility of texture analysis to improve per-pixel classification for high to very high spatial resolution imagery. *International Journal of Remote Sensing*, *26*(4), 733–745. https://doi.org/10.1080/01431160512331316838

Rafferty, J. P., & Pimm, S. L. (2020). Desertification. *Encyclopedia Britannica*. https://www.britannica.com/science/desertification

Rendenieks, Z., Nita, M. D., Nikodemus, O., & Radeloff, V. C. (2020). Half a century of forest cover change along the Latvian-Russian border captured by object-based image analysis of Corona and Landsat TM/OLI data. *Remote Sensing of Environment*, *249*, 112010. https://doi.org/10.1016/j.rse.2020.112010

Rigina, O. (2003). Detection of boreal forest decline with high-resolution panchromatic satellite imagery. *International Journal of Remote Sensing*, *24*(9), 1895–1912. https://doi.org/10.1080/01431160210154894

Robinson, B. E., Li, P., & Hou, X. (2017). Institutional change in social-ecological systems: The evolution of grassland management in Inner Mongolia. *Global Environmental Change*, *47*, 64–75. https://doi.org/10.1016/j.gloenvcha.2017.08.012

Rublee, E., Rabaud, V., Konolige, K., & Bradski, G. (2011). ORB: An efficient alternative to SIFT or SURF. *2011 International Conference on Computer Vision*, 2564–2571. https://doi.org/10.1109/ICCV.2011.6126544

Runnström, M. C. (2000). Is Northern China Winning the Battle against Desertification?: Satellite Remote Sensing as a Tool to Study Biomass Trends on the Ordos Plateau in Semiarid China. *AMBIO: A Journal of the Human Environment*, *29*(8), 468–476. https://doi.org/10.1579/0044-7447-29.8.468

Saleem, A., Corner, R., & Awange, J. (2018). On the possibility of using CORONA and Landsat data for evaluating and mapping long-term LULC: Case study of Iraqi Kurdistan. *Applied Geography*, *90*, 145–154. https://doi.org/10.1016/j.apgeog.2017.12.007

Sandborn, A., & Engstrom, R. N. (2016). Determining the Relationship Between Census Data and Spatial Features Derived From High-Resolution Imagery in Accra, Ghana. *IEEE Journal of Selected Topics in Applied Earth Observations and Remote Sensing*, *9*(5), 1970–1977. https://doi.org/10.1109/JSTARS.2016.2519843

Schlesinger, W. H., Reynolds, J. F., Cunningham, G. L., Huenneke, L. F., Jarrell, W. M., Virginia, R. A., & Whitford, W. G. (1990). Biological Feedbacks in Global Desertification. *Science*, *247*(4946), 1043–1048. JSTOR.

Sghaier, M. O., Foucher, S., & Lepage, R. (2017). River Extraction From High-Resolution SAR Images Combining a Structural Feature Set and Mathematical Morphology. *IEEE Journal of Selected Topics in Applied Earth Observations and Remote Sensing*, *10*(3), 1025–1038. https://doi.org/10.1109/JSTARS.2016.2609804

Shahtahmassebi, A. R., Lin, Y., Lin, L., Atkinson, P. M., Moore, N., Wang, K., He, S., Huang, L., Wu, J., Shen, Z., Gan, M., Zheng, X., Su, Y., Teng, H., Li, X., Deng, J., Sun, Y., & Zhao, M. (2017). Reconstructing Historical Land Cover Type and Complexity by Synergistic Use of Landsat Multispectral Scanner and CORONA. *Remote Sensing*, *9*(7), 682. https://doi.org/10.3390/rs9070682

Shelach, G. (2016). *Prehistoric Societies on the Northern Frontiers of China* (0 ed.). Routledge. https://doi.org/10.4324/9781315539287

Shirkhorshidi, A. S., Aghabozorgi, S., & Wah, T. Y. (2015). A Comparison Study on Similarity and Dissimilarity Measures in Clustering Continuous Data. *PLOS ONE*, *10*(12), e0144059. https://doi.org/10.1371/journal.pone.0144059

Sivakumar, M. V. K. (2007). Interactions between climate and desertification. *Agricultural and Forest Meteorology*, *142*(2–4), 143–155. https://doi.org/10.1016/j.agrformet.2006.03.025

Sohn, H.-G., Kim, G.-H., & Yom, J.-H. (2004). Mathematical modelling of historical reconnaissance CORONA KH-4B Imagery. *The Photogrammetric Record*, *19*(105), 51–66. https://doi.org/10.1046/j.0031-868X.2003.00257.x

Song, D.-X., Huang, C., Sexton, J. O., Channan, S., Feng, M., & Townshend, J. R. (2015). Use of Landsat and Corona data for mapping forest cover change from the

mid-1960s to 2000s: Case studies from the Eastern United States and Central Brazil. *ISPRS Journal of Photogrammetry and Remote Sensing*, *103*, 81–92. https://doi.org/10.1016/j.isprsjprs.2014.09.005

Tao, W. (2014). Aeolian desertification and its control in Northern China. *International Soil and Water Conservation Research*, *2*(4), 34–41. https://doi.org/10.1016/S2095-6339(15)30056-3

Torrione, P. A., Morton, K. D., Sakaguchi, R., & Collins, L. M. (2014). Histograms of Oriented Gradients for Landmine Detection in Ground-Penetrating Radar Data. *IEEE Transactions on Geoscience and Remote Sensing*, *52*(3), 1539–1550. https://doi.org/10.1109/TGRS.2013.2252016

United Nations Convention to Combat Desertification. (2017). *Global Land Outlook*.

United Nations Environmental Programme. (2022, February 10). *From Chile to China: The global battle against desertification*. https://www.unep.org/news-and-stories/story/chile-china-global-battle-against-desertification#:~:text=For%20nearly%2050%20years%2C%20UNEP,take%20coordinated%20action%20against%20desertification.

Unsalan, C. (2006). Gradient-Magnitude-Based Support Regions in Structural Land Use Classification. *IEEE Geoscience and Remote Sensing Letters*, *3*(4), 546–550. https://doi.org/10.1109/LGRS.2006.879560

Verburg, P. H., Crossman, N., Ellis, E. C., Heinimann, A., Hostert, P., Mertz, O., Nagendra, H., Sikor, T., Erb, K.-H., Golubiewski, N., Grau, R., Grove, M., Konaté, S., Meyfroidt, P., Parker, D. C., Chowdhury, R. R., Shibata, H., Thomson, A., & Zhen, L. (2015). Land system science and sustainable

development of the earth system: A global land project perspective. *Anthropocene*, *12*, 29–41. https://doi.org/10.1016/j.ancene.2015.09.004

Wang, T. (2011). *Deserts and aeolian desertification in China*. Science Press.

Wang, T., Song, X., Yan, C., LI, S., & XIE, J. (2011). Remote Sensing Analysis on Aeolian Desertification Trends in Northern China during 1975—2010. *Journal of Desert Research*, *31*(6), 1351–1356.

Wang, T., Yan, C. Z., Song, X., & Xie, J. L. (2012). Monitoring recent trends in the area of aeolian desertified land using Landsat images in China's Xinjiang region. *ISPRS Journal of Photogrammetry and Remote Sensing*, *68*, 184–190. https://doi.org/10.1016/j.isprsjprs.2012.01.001

Wen, Y., Guo, B., Zang, W., Ge, D., Luo, W., & Zhao, H. (2020). Desertification detection model in Naiman Banner based on the albedo-modified soil adjusted vegetation index feature space using the Landsat8 OLI images. *Geomatics, Natural Hazards and Risk*, *11*(1), 544–558. https://doi.org/10.1080/19475705.2020.1734100

Wu, J., Zhang, Q., Li, A., & Liang, C. (2015). Historical landscape dynamics of Inner Mongolia: Patterns, drivers, and impacts. *Landscape Ecology*, *30*(9), 1579–1598. https://doi.org/10.1007/s10980-015-0209-1

Xu, J., Chang, H., Yang, S., & Wang, M. (2012). Fast feature-based video stabilization without accumulative global motion estimation. *IEEE Transactions on Consumer Electronics*, *58*(3), 993–999. https://doi.org/10.1109/TCE.2012.6311347

Xu, L., Tu, Z., Zhou, Y., & Yu, G. (2018). Profiling Human-Induced Vegetation Change in the Horqin Sandy Land of China Using Time Series Datasets. *Sustainability*, *10*(4), 1068. https://doi.org/10.3390/su10041068

Xue, Z., Kappas, M., & Wyss, D. (2021). Spatio-Temporal Grassland Development in Inner Mongolia after Implementation of the First Comprehensive Nation-Wide Grassland Conservation Program. *Land*, *10*(1), 38. https://doi.org/10.3390/land10010038

Yang, K., Li, M., Liu, Y., Cheng, L., Huang, Q., & Chen, Y. (2015). River Detection in Remotely Sensed Imagery Using Gabor Filtering and Path Opening. *Remote Sensing*, *7*(7), 8779–8802. https://doi.org/10.3390/rs70708779

Yi, B., & Zhang, L. (2011). The cultivation of inner Mongolia and its effect on the ecological environment since the qing dynasty (in Chinese). *Collect. Pap. Hist. Stud.*, *5*, 88–96.

Zanaga, Daniele, Van De Kerchove, Ruben, De Keersmaecker, Wanda, Souverijns, Niels, Brockmann, Carsten, Quast, Ralf, Wevers, Jan, Grosu, Alex, Paccini, Audrey, Vergnaud, Sylvain, Cartus, Oliver, Santoro, Maurizio, Fritz, Steffen, Georgieva, Ivelina, Lesiv, Myroslava, Carter, Sarah, Herold, Martin, Li, Linlin, Tsendbazar, Nandin-Erdene, … Arino, Olivier. (2021). *ESA WorldCover 10 m 2020 v100* (Version v100) [Data set]. Zenodo. https://doi.org/10.5281/ZENODO.5571936

Zhang, G., Dong, J., Xiao, X., Hu, Z., & Sheldon, S. (2012). Effectiveness of ecological restoration projects in Horqin Sandy Land, China based on SPOT-VGT NDVI data. *Ecological Engineering*, *38*(1), 20–29. https://doi.org/10.1016/j.ecoleng.2011.09.005

Zhang, Q., Wang*, J., Gong, P., & Shi, P. (2003). Study of urban spatial patterns from SPOT panchromatic imagery using textural analysis. *International Journal of Remote Sensing*, *24*(21), 4137–4160. https://doi.org/10.1080/0143116031000070445

Zhang, Y., Shen, W., Li, M., & Lv, Y. (2020). Integrating Landsat Time Series Observations and Corona Images to Characterize Forest Change Patterns in a Mining Region of Nanjing, Eastern China from 1967 to 2019. *Remote Sensing*, *12*(19), 3191. https://doi.org/10.3390/rs12193191

Zhou, Y., Chang, X., Ye, S., Zheng, Z., & Lv, S. (2015). Analysis on regional vegetation changes in dust and sandstorms source area: A case study of Naiman Banner in the Horqin sandy region of Northern China. *Environmental Earth Sciences*, *73*(5), 2013–2025. https://doi.org/10.1007/s12665-014-3566-1